

---

# DISENTANGLING EMBEDDING SPACES WITH MINIMAL DISTRIBUTIONAL ASSUMPTIONS

---

**Tobias Leemann\***

University of Tübingen  
tobias.leemann@uni-tuebingen.de

**Michael Kirchhof\***

University of Tübingen  
michael.kirchhof@uni-tuebingen.de

**Yao Rong**

University of Tübingen  
yao.rong@uni-tuebingen.de

**Enkelejda Kasneci**

University of Tübingen  
enkelejda.kasneci@uni-tuebingen.de

**Gjergji Kasneci**

University of Tübingen  
gjergji.kasneci@uni-tuebingen.de

## ABSTRACT

Interest in understanding and factorizing learned embedding spaces is growing. For instance, recent concept-based explanation techniques analyze a machine learning model in terms of interpretable latent components. Such components have to be discovered in the model’s embedding space, e.g., through independent component analysis (ICA) or modern disentanglement learning techniques. While these unsupervised approaches offer a sound formal framework, they either require access to a data generating function or impose rigid assumptions on the data distribution, such as independence of components, that are often violated in practice. In this work, we link conceptual explainability for vision models with disentanglement learning and ICA. This enables us to provide first theoretical results on how components can be identified without requiring any distributional assumptions. From these insights, we derive the *disjoint attributions (DA)* concept discovery method that is applicable to a broader class of problems than current approaches, but yet possesses a formal identifiability guarantee. In an extensive comparison against component analysis and over 300 state-of-the-art disentanglement models, DA stably maintains superior performance, even under varying distributions and correlation strengths.

## 1 Introduction

Modern computer vision systems represent images in high-dimensional embedding spaces. To unveil why an image is considered to be similar to a certain class, interest in understanding these embeddings, e.g., via conceptual explanations [25, 28, 12, 47, 1, 22], is increasing. The goal is to scrutinize a given encoder by decomposing its embedding space into individual directions which correspond to exactly one interpretable concept of an image at a time. Yet, the problem of concept discovery, i.e., finding such interpretable directions, is hard and its definition is still a topic of discussion [31, 47].

Concurrently, disentanglement learning [17, 8, 32] offers a more formal perspective on the problem. Here, it is also assumed that there exist interpretable ground-truth components, which are analogous to concepts from a conceptual explanations viewpoint [23]. The images are seen as random samples from the distribution of these components, which are decoded into the image-domain via an image-generating process. The goal is to subsequently build a generative model and an embedding-space that is *disentangled*, i.e., each latent dimension corresponds to precisely one ground-truth component. There is a growing body of literature on the conditions under which this can be theoretically

---

\*Equal contribution

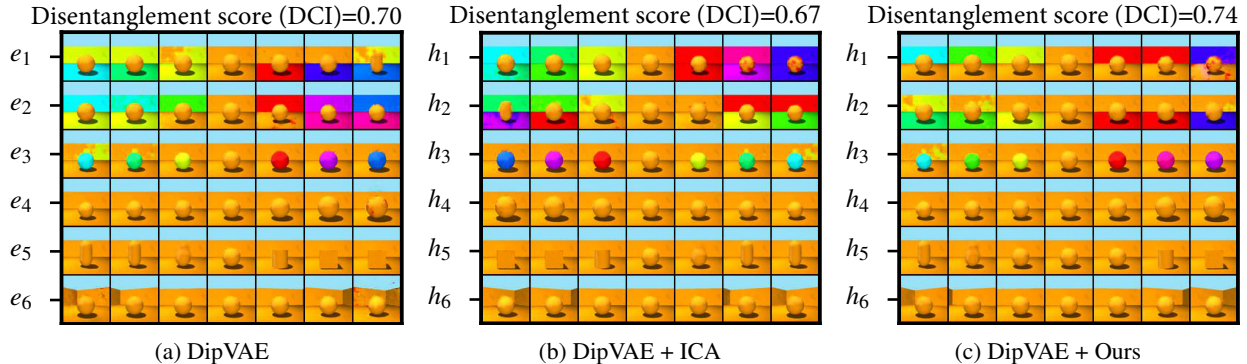


Figure 1: (a) Traversals along each embedding space axis  $e_k$  of the best model (DipVAE) trained on correlated components. DipVAE struggles to disentangle the components *floor color* and *background color* to  $e_1$  and  $e_2$  individually. Precisely, it embeds them in almost parallel directions. (b) Because of the correlation and the isotropic structure of the embedding space, ICA fails to find these directions  $h_k$  post-hoc. (c) Our disjoint attributions approach is able to separate the components into  $h_1$  and  $h_2$ .

guaranteed [21, 18, 48], which are known as *identifiability* conditions. Drawing from classical independent component analysis (ICA) [10, 20], a key ingredient of most of these proofs is the assumption of stochastic independence of the ground-truth components besides other distributional assumptions such as non-Gaussianity [20, 19, 18]. Recently, Träuble et al. [43] have shown how strongly current disentanglement learning methods depend on these distributional assumptions, since they fail even if just two components of a dataset are correlated. Fig. 1a shows an example: If we move along the unit directions  $e_1, e_2$  in the embedding space of this state-of-the-art disentanglement model, the (correlated) components *floor color* and *background color* should change independently. This is not fulfilled, and likewise the directions  $h_k$  that ICA discovers post-hoc are not disentangled either (Fig. 1b). This sensitivity to the independence assumption and the fact that disentanglement learning usually requires building a generator and cannot be applied post-hoc to a given discriminative classifier, makes current approaches unsuitable for the concept discovery setting. Instead, we seek a powerful concept discovery approach that is (1) robust to distributional assumptions such as correlated factors, (2) applicable to latent spaces of trained classifiers post-hoc, and (3) has a theoretical identifiability guarantee, thus mapping each discovered concept to precisely one meaningful ground-truth component.

To date, there is no such method. Yet, the close bond between disentanglement and concept discovery begs the question: *Can the identifiability guarantees of disentangled generators be transferred to (possibly discriminative) encoders without making restrictive distributional assumptions?* Intuitively, ICA identifies the ground-truth concepts via *traces* that their latent distribution leaves in the embedded data. To become independent of such distributional properties, we need to search for similar traces in *how* the images are generated from the ground-truth concepts from a functional perspective. Indeed, recent disentanglement learning literature studies properties such as independent mechanisms [15].

In this work, we show that such a trace imprinted on the functional form of the data-generating process will also be visible in how a given encoder processes the data. Yet, we show that the prominent independent mechanisms property leaves no distinct enough trace. Thus, we propose a novel property on the data-generating process, and prove that its trace within corresponding encoders, termed *disjoint attributions (DA)*, is strong enough to ensure identifiability of the disentangled components.

In summary, our work offers the following contributions: **(1)** We propose a *transfer lemma* that transfers functional traces from the disentanglement literature to encoder embedding spaces. **(2)** We propose the *disjoint attributions* criterion and prove the disentanglement of the original components up to permutation and scale. **(3)** We utilize DA for a concept discovery algorithm for encoder embedding spaces that has a theoretical identifiability guarantee without requiring distributional assumptions. **(4)** To test its identifiability promise in practice, we first apply it to the aforementioned correlated disentanglement setting [43], where it shows increased performance against an extensive collection of state-of-the-art disentanglement approaches [17, 26, 30]. The performance is upheld across datasets and various correlations and even when approaches are composed with post-hoc ICA. **(5)** We put DA to the test with an encoder trained on a purely discriminative task and further apply it on the high-dimensional, real-world CUB-200-2011 dataset [45] with a ResNet50 [16] classifier.

## 2 Related work

From the multitude of works conducted on the identification and interpretation of components in latent spaces, our work is motivated by conceptual explanations but technically closest to the domains of disentanglement learning and ICA. We briefly review these domains in the following paragraphs.

**Concept discovery for explainable AI.** Recently, conceptual explanations [28, 25, 12, 47, 1] have gained popularity within the XAI community. They constitute a novel explanation technique that aims to explain a trained machine learning model post-hoc in terms of human-friendly, high-level concepts [25]. These concepts are sometimes provided along with the dataset in different forms of annotations [28, 26, 22], whereas other works rely on clustering techniques to solve the more general unsupervised case [12, 47, 1]. However, there are no theoretical guarantees for identifiability and the results are not always meaningful [31, 47]. Our approach can be used for unsupervised concept discovery and has a formal guarantee on identifiability rooted in disentanglement learning.

**Disentanglement and ICA.** The goal of disentanglement learning is finding a data-generating mechanism  $g(z)$  and a latent representation  $z$  for a dataset, such that each of the original components (also known as factors of variation) is mapped to one (controllable) unit direction in  $z$  [4]. Most works in the domain enhance VAEs [27] with additional loss terms [17, 8, 26, 9, 30]. ICA [10, 20, 19] or blind source separation (BSS) view  $g(z)$  as a mixture to undo and rely on traces that the distributions over  $z$  leave in the mixture. Both domains require independence of the underlying components, which is often not applicable in naturally correlated processes. This fundamental problem was only recently addressed and shown to break current disentanglement learning approaches [43]. Hence, we design a distribution-agnostic method that is applicable even in correlated settings and outside VAEs.

**Identifiability results.** It has been previously shown that unsupervised disentanglement, without further assumptions, is impossible [20, 32]. However, one way to make it feasible is to add additional supervision. Identifiability has been shown when having access to an additional observed variable [21, 24] or to tuples of observations that differ in only a limited number of components [33]. Another strain of work constrains the form of the generating process. Horan et al. [18] showed that the assumption of isometry for the generating process together with non-Gaussian distributed, independent components suffices to identify a disentangled representation. Recently, Gresele et al. [15] and Zheng et al. [48] introduced a functional independence assumption on the data generator, that requires the output changes for infinitesimal variations in each component to be orthogonal to each other. However, [15, 48] only consider the case of independently distributed components and assume access to a generator function, which limits the applicability of their methods to discriminatively or contrastively trained embedding spaces. Our work fills this gap by providing initial results for the most general case without distributional assumptions and transfers them to encoder-only setups.

## 3 Identifiability without distributional assumptions

The aim of this section is to find a distribution-agnostic trace that a concept discovery method can utilize to guarantee the identification of disentangled components. To this end, we first formalize the problem (Sec. 3.1). Then, we transfer the independent mechanism principle from disentanglement learning to our setting and show that it is insufficient to guarantee identifiability (Sec. 3.2). Consequently, we strengthen it and derive the *disjoint attributions* criterion. We prove that it enables a concept discovery method to identify disentangled components (Sec. 3.3).

### 3.1 Problem formalization

Let us first formalize the problem setup visualized in Fig. 2. Let there be  $K$  ground-truth components whose scores are stored in  $z \in \mathcal{Z} \subset \mathbb{R}^K$ . Let there further be a function  $g : \mathcal{Z} \rightarrow \mathcal{X}$  that generates images  $x = g(z) \in \mathcal{X} \subset \mathbb{R}^L$  from the components  $z$ , where  $L \gg K$ . Let there be a known encoder  $f : \mathcal{X} \rightarrow \mathcal{E}$  that we want to scrutinize, where  $e = f(x) \in \mathcal{E} \subset \mathbb{R}^K$  is the embedding of each image. We suppose that  $f$  is differentiable, so that Jacobians  $J_f(x)$  exist, at least for all  $x \in \{g(z) | z \in \mathcal{Z}\}$ .

To be able to disentangle the original components, we first need to assume that they all exist in  $f$ 's embedding space, albeit in unknown linear directions. That is,  $(f \circ g)(z) = Dz$ , where  $D \in \mathbb{R}^{K \times K}$ . As a shorthand, we write  $f \circ g = D$ , where  $D$  also refers to the corresponding linear operator. This linearity is common in interpretability literature [25, 47] and based on the frequent observation that concepts tend to be linearly encoded in embedding spaces [42, 3, 2, 5]. A linear de-mixture operation  $M \in \mathbb{R}^{K \times K}$  is said to *disentangle* the original concepts if it undoes the effect of  $D$ , i.e., after applying it to the embeddings, each dimension of  $Me$  corresponds to a component dimension in  $z$ . Formally, we want that  $Mf \circ g = PS$ , where  $P \in \mathbb{R}^{K \times K}$  is a permutation matrix that has one 1 per row and column and is otherwise 0, and  $S \in \mathbb{R}^{K \times K}$  is a diagonal scaling matrix.

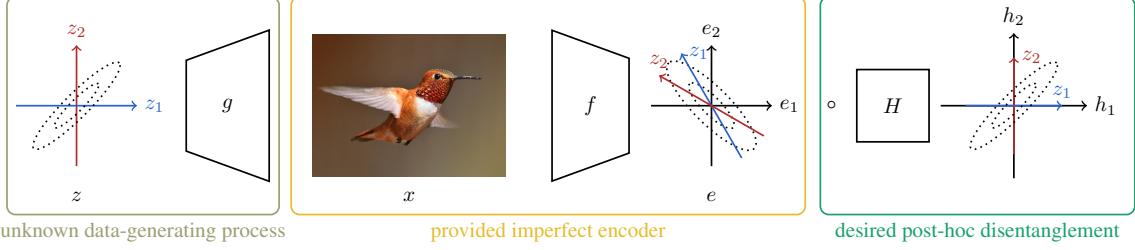


Figure 2: The decoder-encoder setup linking the latent concepts (left) to the given embedding space (center). A post-hoc disentanglement allows re-identifying the original concepts (right).

We seek a method that provably delivers such a disentangled de-mixing operation, i.e., that *identifies* it among all possible operations. Besides just the embeddings  $\{e_n\}_{n=1,\dots,N}$ , we also provide this method the  $N$  images  $\{x_n\}_{n=1,\dots,N}$  and the (imperfect) encoder  $f$ . This task can be seen as a linear ICA problem on the mixture  $f \circ g$ , but there are some distinctive characteristics due to our embedding-space motivation that render the problem unidentifiable by existing approaches:

1. The distribution  $p(z)$  is unconstrained. Inter alia, the components may be correlated and Gaussian and thus the method cannot rely on distributional traces to disentangle them.
2.  $g$  is an unknown and complicated function "of nature", and we will not approximate it. Therefore, we have to utilize traces imprinted on it in an indirect way.
3. Both  $g$  and  $f$  are non-linear functions.
4. Our approach is unsupervised in terms of  $z$ .

### 3.2 Independent mechanisms do not ensure identifiability

With these constraints, we will have to try to find traces in the functional properties of the encoder  $f$  that allow disentangling the original components. To this end, let us first define how an ideal encoder  $f^*$  that is already disentangled would look like.

**Definition 3.1** (Minimal disentangled encoder (MDE)). *Let  $g$  be fixed.  $f^* : \mathcal{X} \rightarrow \mathcal{E}$  is a minimal disentangled encoder (MDE) of  $g$  if:*

1.  $f^* \circ g = PS$ , where  $P \in \mathbb{R}^{K \times K}$  is a permutation and  $S \in \mathbb{R}^{K \times K}$  is a scaling matrix.
2.  $f^*$  has minimal total variation (min TV) within  $\mathfrak{F} := \{f | f \circ g = PS\}$  [6].

The principle of total variation [36] and the variant for vectorized functions that we use [6], stem from classical computer vision. It constrains the norm of the gradients to be minimal and can be seen a technical condition for the upcoming proofs. Intuitively, it ensures that  $f^*$  does not rely on component-unrelated information, such as noise, in the high-dimensional image space ( $L \gg K$ ).

Since  $f \circ g = D$ , in our case,  $f^*$  will be a linearly processed form of the given  $f$ , i.e.  $f^* = Mf$ , but for the sake of generality, let us first understand  $f^*$  and  $g$  as arbitrary encoders and decoders. As previously discussed, we will not be able to use functional traces in  $g$  directly. Thus, we first need a way to transfer these properties to  $f^*$ . This is done by the following lemma which shows that if  $f^*$  is an MDE of  $g$ , they must share the structure of their Jacobians.

**Lemma 3.1** (Transfer lemma). *Let  $g$  be fixed and let  $f^*$  be an MDE of  $g$ , where both Jacobians  $J_{f^*}(g(z)) \in \mathbb{R}^{K \times L}$  and  $J_g(z) \in \mathbb{R}^{L \times K}$  exist  $\forall z \in \mathcal{Z}$ . Then,  $J_{f^*}(g(z)) = PSJ_g(z)^\top \forall z \in \mathcal{Z}$ , where  $P \in \mathbb{R}^{K \times K}$  is a permutation and  $S \in \mathbb{R}^{K \times K}$  is a diagonal matrix.*

**Proof idea.** Since  $f^* \circ g = PS$ , the Jacobians behave analogously. Further, the min TV condition of  $f^*$  prevents  $J_{f^*}$  from containing kernel elements of  $J_g$ . The detailed proof is in Appendix B.1.  $\square$

Intuitively, this lemma says that if the original concepts leave a trace on the structure of the Jacobian of  $g$ , this trace is also imprinted on the Jacobian  $J_{f^*}$  of any MDE  $f^*$ . Concretely, one such trace that natural generators are argued to fulfill [15] is the independent mechanisms property:

**Definition 3.2** (Independent mechanisms (IMA)).  $g$  is said to generate  $x$  from its components  $z$  via independent mechanisms if the Jacobian  $J_g(z)$  of  $g$  exists and its columns (one per component) are orthogonal  $\forall z \in \mathcal{Z}$ , i.e.,  $J_g^\top(z)J_g(z) = S$ , where  $S \in \mathbb{R}^{K \times K}$  is a diagonal matrix. [15]

The transfer lemma allows to directly transfer this functional characteristic to an MDE encoder.

**Corollary 3.1** (Orthogonal attributions (OA)). If  $g$  adheres to IMA, then the Jacobian  $J_{f^*}(g(z))$  of any MDE  $f^*$  must have orthogonal rows  $\forall z \in \mathcal{Z}$ , that is,  $J_{f^*}(g(z))J_{f^*}(g(z))^\top = S$ , where  $S \in \mathbb{R}^{K \times K}$  is a diagonal matrix.

Now we have a characteristic property at hand that an MDE  $f^*$  necessarily fulfills. We could use this trace in our problem setup to find a de-mixture matrix  $H$  that has OA. However, this search would not be guaranteed to identify the MDE matrix  $M$  that disentangles the components, since an  $H$  with the OA property actually can only be guaranteed to find any *rotated* (and scaled) version of  $M$ , which breaks the axis-alignment of the disentangled components of  $Mf$ :

**Theorem 3.1** (Non-identifiability under IMA). Let  $g$  adhere to IMA. Let  $f$  be given with  $f \circ g = D$ , where both  $J_f(g(z))$  and  $J_g(z)$  exist  $\forall z \in \mathcal{Z}$ . If there exists an MDE  $f^* = Mf$ , where  $M \in \mathbb{R}^{K \times K}$  has full rank, then an  $f' = Hf$  with a full-rank  $H \in \mathbb{R}^{K \times K}$  and orthogonal rows in its Jacobian  $J_{f'}(g(z)) \forall z \in \mathcal{Z}$  must be a rotated, scaled version of  $f^*$ . I.e.,  $H = RSM$ , where  $R \in \mathbb{R}^{K \times K}$  is an orthogonal rotation and  $S \in \mathbb{R}^{K \times K}$  is a diagonal scaling matrix.

**Proof idea.** With Corollary 3.1, an MDE of an IMA process must have orthogonal rows in its Jacobian. Indeed, this can only be achieved if  $H$  is a rotated and scaled  $M$ . However, the MDE property of  $Mf$  is only preserved by permutations and scales. The detailed proof is given in Appendix B.2.  $\square$

### 3.3 Disjoint mechanisms ensure identifiability

The previous theorem means that the trace that the IMA condition leaves is too weak to ensure identifiability in our problem setup. However, to obtain a more distinct trace, it suffices to slightly strengthen the IMA condition. This results in the *disjoint mechanisms* principle.

**Definition 3.3** (Disjoint mechanisms (DMA)).  $g$  is said to generate  $x$  from its components  $z$  via disjoint mechanisms if the Jacobian  $J_g(z)$  exists and is a block matrix  $\forall z \in \mathcal{Z}$ . That is, the columns of  $J_g(z)$  are non-zero at disjoint rows, i.e.  $|J_g(z)|^\top |J_g(z)| = S$ , where  $S \in \mathbb{R}^{K \times K}$  is a diagonal matrix and  $|\cdot|$  takes the element-wise absolute value.

Note that each DMA process is also IMA. Thus, we now have a strengthened property at hand and we can again apply the transfer lemma to obtain a stronger characteristic trace for  $f^*$ .

**Corollary 3.2** (Disjoint attributions (DA)). If  $g$  adheres to DMA, then the rows of the Jacobian  $J_{f^*}(g(z))$  of any MDE  $f^*$  must be disjoint  $\forall z \in \mathcal{Z}$ , that is,  $|J_{f^*}(g(z))| |J_{f^*}(g(z))|^\top = S$ , where  $S \in \mathbb{R}^{K \times K}$  is a diagonal scaling matrix and  $|\cdot|$  takes the element-wise absolute value.

Indeed, as opposed to OA, this is not only a necessary property of  $f^*$ , but a trace that *only* an MDE shows. Thus, we can identify a disentangled  $M$  by checking which  $H$  fulfills that  $Hf$  has DA.

**Theorem 3.2** (Identifiability under DMA). Let  $g$  adhere to DMA. Let  $f$  be given with  $f \circ g = D$ , where both  $J_{f^*}(g(z))$  and  $J_g(z)$  exist  $\forall z \in \mathcal{Z}$ . If there exists an MDE  $f^* = Mf$ , where  $M \in \mathbb{R}^{K \times K}$  has full rank, then an  $f' = Hf$  with a full-rank  $H \in \mathbb{R}^{K \times K}$  and disjoint rows in its Jacobian  $J_{f'}(g(z)) \forall z \in \mathcal{Z}$  must be an MDE.

**Proof idea.** Corollary 3.2 yields that an MDE of a DMA process must have disjoint rows in its Jacobian. In fact, the only matrices  $H$  that lead to orthogonal rows are permutations and scales of  $M$ . Hence,  $Hf$  must be an MDE itself. The detailed proof is in Appendix B.3.  $\square$

**In summary,** the DMA condition on  $g$ , other than IMA, is sufficient to ensure that an  $f' = Hf$  with disjoint rows in its Jacobian will be an MDE and will thus disentangle the components in our problem setup. This property can be used as a functional trace to identify the de-mixture matrix  $M$ .

## 4 Efficient post-hoc disentanglement via disjoint attributions

In this section, we give an efficient implementation for a method that identifies MDEs via the DA property. Further, we generalize our method and motivate why it is named *disjoint attributions*.

Suppose again that we are provided with a trained encoder  $f : \mathbb{R}^L \rightarrow \mathbb{R}^K$  with existing Jacobians  $J_f(x) \in \mathbb{R}^{K \times L}$  and  $N$  images  $\{x_n\}_{n=1, \dots, N}$ . Let  $H \in \mathbb{R}^{K \times K}$  be a matrix that contains  $K$  directions in the latent space, one in each

row. The function  $Hf(x)$  projects the output of  $f$  to the directions contained in  $H$ , thus giving scores for each found component. To disentangle the original components, we now optimize for the matrix  $H$  that leads to the most disjoint Jacobians  $J_{Hf}(x)$ , i.e.,

$$\min_H \sum_{n=1}^N \left\| \left| \overline{J_{Hf}(x)} \right| \left| \overline{J_{Hf}(x)} \right|^\top - I_K \right\|_F^2. \quad (1)$$

An important detail is that  $\overline{\cdot}$  denotes the row-wise normalization to unit length. Thus, the above comparison to the unit matrix  $I_K$  ensures that off-diagonal elements are zero, which is the disjointness property, and diagonal elements are non-zero. This rules out solutions where  $H$  has no full rank or even  $H = 0$ , but does not constraint the scale and thus does not enforce, e.g., an isometry.

So far, the objective is unsuitable for optimization with gradient descent, as computing its gradient w.r.t.  $H$  would require deriving the Jacobian, demanding second-order gradients. However, since  $J_f$  is homogeneous, i.e.,  $J_{Hf}(x) = HJ_f(x)$ , we can rearrange the terms such that the Jacobians are independent of  $H$  (and thus, constants in the optimization), which allows for efficient optimization:

$$\min_H \sum_{n=1}^N \left\| \left| \overline{HJ_f(x)} \right| \left| \overline{HJ_f(x)} \right|^\top - I_K \right\|_F^2. \quad (2)$$

Now, intuitively,  $J_f = \nabla_x(f(x))$  contains input gradients (termed *grad* in the remainder) which can be thought of as a simple form of attribution for each component [39, 38]. Thus, on a more general level, our proposed approach optimizes for the disjointness of attributions. This corresponds to the intuition that the original components control independent aspects of the image and that their attributions, which reflect their most influenced image regions, should thus also be independent. Thus, we may use other forms of *homogeneous attributions* in place of  $J_f$ . These are local attribution methods  $A_f : \mathbb{R}^L \rightarrow \mathbb{R}^{K \times L}$  for the encoder  $f$  with  $A_{Hf}(x) = HA_f(x)$  that map an instance  $x$  to a matrix of attributions for each latent dimension. Besides the above input gradients, this class contains other popular methods such as integrated gradients (IG) [41] and smoothed gradients (SG) [40] (cf. Appendix B.4 for a proof). Thus, we can formulate a generalized *disjoint attributions objective*:

$$\min_H \sum_{n=1}^N \left\| \left| \overline{HA_f(x)} \right| \left| \overline{HA_f(x)} \right|^\top - I_K \right\|_F^2. \quad (3)$$

Note that one can remove the absolute value to obtain an *orthogonal attributions objective* based on IMA. DA fulfills the three desiderata established in the introduction, i.e., distributional robustness, post-hoc applicability, and a theoretical identifiability guarantee. Thereby, it is able to discover disentangled components that can be easily mapped to semantically meaningful real-world concepts.

## 5 Experiments

To put these theoretical insights to a practical test, we conduct a large-scale comparison of DA to component analysis and disentanglement approaches on two correlated datasets (Sec. 5.2). We further study its robustness under increasing correlations and distributional challenges (Sec. 5.3) as well as in embedding spaces of discriminatively trained encoders (Sec. 5.4). Finally, we scale up from these controlled experiments and make an initial attempt on the real-world CUB-200-2011 (Sec. 5.5).

### 5.1 Experimental setup

Across the first three experiments, we use correlated versions of the common Shapes3D [7] as well as the recently published MPI3D-real dataset [13]. These datasets show images of objects that vary in 6, resp. 7, components describing their colors, shape, orientation, and background. These ground truths are not leveraged at train time but allow quantifying the disentanglement of the estimated to the true components through the DCI score [11] implemented in the `disentanglement_lib` [32]. Results in other metrics are shown in the appendix. In a fourth experiment, we evaluate on CUB-200-2011 [45] (cf. Appendix C.5). Unless otherwise noted, we used SG attributions [40] for our method, which we found to deliver the most stable results. In the first two experiments, we obtain the embedding spaces from four disentanglement variants of VAEs (BetaVAE [17], FactorVAE [26], BetaTCVAE [9], DipVAE [30]) from a recent study [32] with equal encoder and decoder architectures (cf. Appendix C.2). In the latter two experiments, we use discriminative models. They are trained on five random initialization seeds with hyperparameters tuned via grid-search (cf. Appendix C.6). In total, we trained and disentangled 315 models, requiring about 124 Nvidia RTX2080Ti GPU days.

Dataset	Shapes3D			MPI3D-real		
	Correlated factors	floor vs. background	orientation vs. background	orientation vs. size	background vs. object color	background vs. robot arm dof-1
<b>BetaVAE</b>	0.497 ± 0.028	0.581 ± 0.044	0.491 ± 0.049	0.340 ± 0.027	0.277 ± 0.026	0.300 ± 0.046
+PCA	0.258 ± 0.028	0.330 ± 0.029	0.314 ± 0.040	0.116 ± 0.008	0.174 ± 0.021	0.154 ± 0.015
+ICA	0.569 ± 0.043	0.526 ± 0.084	0.576 ± 0.039	0.237 ± 0.042	0.205 ± 0.023	0.180 ± 0.021
+Ours (OA)	0.438 ± 0.127	0.605 ± 0.049	0.583 ± 0.030	<b>0.355 ± 0.033</b>	<b>0.349 ± 0.015</b>	<b>0.337 ± 0.038</b>
+Ours (DA)	<b>0.593 ± 0.094</b>	<b>0.623 ± 0.054</b>	<b>0.626 ± 0.031</b>	0.334 ± 0.025	0.317 ± 0.028	0.278 ± 0.030
<b>FactorVAE</b>	0.507 ± 0.105	0.502 ± 0.076	0.712 ± 0.010	<b>0.205 ± 0.022</b>	<b>0.239 ± 0.017</b>	0.171 ± 0.005
+PCA	0.361 ± 0.074	0.481 ± 0.050	0.560 ± 0.033	0.179 ± 0.010	0.234 ± 0.012	0.171 ± 0.006
+ICA	0.294 ± 0.071	0.268 ± 0.050	0.305 ± 0.073	0.066 ± 0.009	0.090 ± 0.006	0.073 ± 0.011
+Ours (OA)	0.561 ± 0.040	<b>0.509 ± 0.033</b>	<b>0.587 ± 0.051</b>	0.201 ± 0.019	0.226 ± 0.010	<b>0.191 ± 0.011</b>
+Ours (DA)	<b>0.600 ± 0.027</b>	0.493 ± 0.044	0.575 ± 0.029	0.184 ± 0.013	0.218 ± 0.016	0.180 ± 0.013
<b>BetaTCVAE</b>	0.619 ± 0.008	0.613 ± 0.041	0.659 ± 0.005	<b>0.383 ± 0.022</b>	<b>0.359 ± 0.026</b>	<b>0.309 ± 0.036</b>
+PCA	0.402 ± 0.029	0.422 ± 0.067	0.443 ± 0.063	0.356 ± 0.022	0.328 ± 0.017	0.295 ± 0.038
+ICA	0.567 ± 0.014	0.478 ± 0.046	0.619 ± 0.022	0.245 ± 0.041	0.260 ± 0.024	0.170 ± 0.045
+Ours (OA)	0.620 ± 0.021	0.643 ± 0.026	0.637 ± 0.037	0.323 ± 0.025	0.316 ± 0.029	0.271 ± 0.033
+Ours (DA)	<b>0.670 ± 0.014</b>	<b>0.667 ± 0.021</b>	<b>0.749 ± 0.027</b>	0.327 ± 0.027	0.325 ± 0.025	0.272 ± 0.033
<b>DipVAE</b>	0.631 ± 0.018	0.652 ± 0.017	0.548 ± 0.036	0.235 ± 0.019	0.181 ± 0.049	0.232 ± 0.040
+PCA	0.148 ± 0.012	0.165 ± 0.018	0.188 ± 0.027	0.090 ± 0.005	0.088 ± 0.028	0.091 ± 0.011
+ICA	0.629 ± 0.018	0.651 ± 0.017	0.542 ± 0.033	0.234 ± 0.019	0.180 ± 0.048	0.232 ± 0.041
+Ours (OA)	0.642 ± 0.017	0.615 ± 0.017	0.562 ± 0.050	0.230 ± 0.022	0.182 ± 0.048	0.230 ± 0.042
Ours (DA)	<b>0.682 ± 0.010</b>	<b>0.682 ± 0.013</b>	<b>0.601 ± 0.055</b>	<b>0.249 ± 0.026</b>	<b>0.188 ± 0.049</b>	<b>0.253 ± 0.051</b>

Table 1: Mean ± std. err. of the DCI scores of different post-hoc methods applied to the embedding spaces of four disentanglement models on two datasets with different pairs of correlated variables.

## 5.2 Rectifying disentanglement models learned from correlated data

We first consider the setup of [43] where the datasets are resampled such that two components  $z_i, z_j \in [0, 1]$  follow  $z_i - z_j \sim \mathcal{N}(0, s^2)$ . Lower  $s$  results in a stronger correlation where only few pairs of component values co-occur frequently. We train the disentanglement models on these resampled datasets and subsequently apply ICA, PCA, and our DA and OA methods on their embedding spaces ( $K \in \{6, 7\}$ ). They are challenged with different pairs of correlated components, e.g., nominal/nominal, nominal/ordinal, ordinal/ordinal, and those encoded in the same image areas.

Tab. 1 shows the DCI scores for a moderate correlation of  $s = 0.4$ . Note that differences as small as 0.05 in the metric can mean a big improvement in disentanglement (cf. Figure 1), because the metric is computed across all components but disentanglement might already be achieved for the non-correlated components. On Shapes3D, DA outperforms the baselines on all but one setup, impressively highlighting that it works regardless of the disentanglement method used and components correlated. Within our approaches, DA outperforms OA on all but one setup on Shapes3D. On the more challenging MPI3D-real dataset, the rather shallow encoder and decoder architectures of the disentanglement models struggle to reconstruct the images (cf. Appendix D.1) and thus offer a low disentanglement in their embeddings. However, DA still leads to improvement for the BetaVAE model and the DipVAE model, while PCA and ICA beat neither the plain model nor DA.

## 5.3 Sensitivity to Gaussianity and multiple correlations

In this section, we test the robustness of our approach to stronger distributional challenges to analyze whether it is as distribution-agnostic as the theory predicts. To this end, we lay a Gaussian prior over the components of the Shapes3D dataset (cf. Appendix C.2) which contains correlations  $\rho$ .

First, we increase the correlation strength between floor and background color. In Fig. 3, the BetaVAE handles low correlations well but starts deteriorating from a strength of  $\rho > 0.5$ , along with ICA. The DCI of our methods is an average constant of +0.145 above the BetaVAE’s for  $\rho \leq 0.85$ . After this, it returns to the BetaVAE’s DCI, possibly because the two components collapsed in the underlying BetaVAE’s embedding space. For Fig. 3b, we gradually added more moderately correlated pairs to the Gaussian’s covariance matrix until eventually all components were correlated. Again, our models show a constant benefit over the underlying BetaVAE’s DCI curve. This demonstrates that a post-hoc method’s performance depends on the underlying model but that it can outperform it consistently. A second observation is that BetaVAE’s and ICA’s initial decay is faster than in the previous experiment. This reveals their struggle in settings where multiple components are naturally correlated.

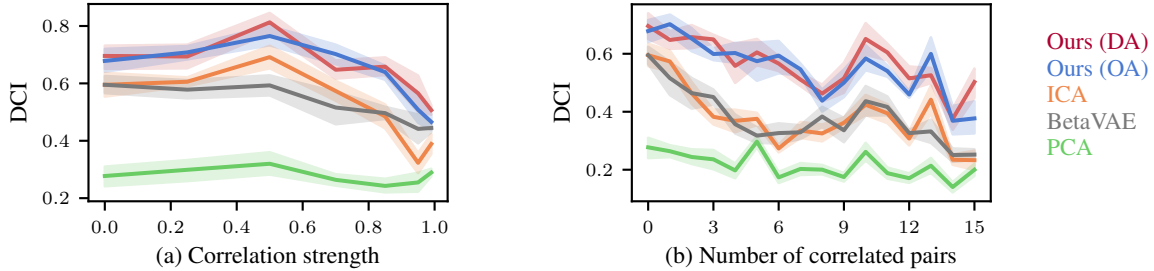


Figure 3: Robustness under Gaussian prior and increasing pairwise correlations between concepts. Shaded areas show the standard deviation of the mean over five seeds. Best viewed in color.

## 5.4 Discriminative latent spaces

A fundamental advantage of our approach over disentanglement learning is that it can be applied post-hoc to latent spaces of classification models that were trained in a purely discriminative manner, e.g., the feature space of a CNN model. To investigate this setting, we set up an 8-class classification problem on the Shapes3D dataset, where the combination of the four binarized components object color, wall color (blue/red vs. yellow/green), shape (cylinder vs. cube) and orientation (left vs. right) determines the class (cf. Appendix C.3). To make the setting even more realistic, we artificially add labeling noise close to the decision boundary, correlations as in Sec. 5.2, and an L2-regularizer on the embeddings to constrain them to a reasonable range. We train a simple CNN with a  $K=6$ -dimensional embedding space before the final classification layer.

The discriminative loss leads to a clustered distribution in the embedding space. Tab. 2 shows that ICA expectedly works very well in this highly non-Gaussian distribution. However, tables turn as we increasingly correlate the floor and background color: Starting at  $s = 0.2$ , DA significantly outperforms ICA. This demonstrates that our method is applicable to purely discriminative latent spaces and, in line with the previous experiment, that it is more robust to correlations than ICA.

Method	$s = 0.1$	$s = 0.2$	$s = 0.4$
unit dirs.	$0.237 \pm 0.01$	$0.249 \pm 0.01$	$0.232 \pm 0.01$
PCA	$0.238 \pm 0.01$	$0.371 \pm 0.03$	$0.226 \pm 0.01$
ICA	$0.411 \pm 0.02$	$0.313 \pm 0.01$	<b><math>0.530 \pm 0.16</math></b>
Ours (DA, IG)	<b><math>0.468 \pm 0.05</math></b>	<b><math>0.447 \pm 0.03</math></b>	$0.412 \pm 0.03$

Table 2: Mean  $\pm$  std. err. of the DCI scores for concept discovery in a discriminative latent space.

## 5.5 Real-world concept discovery

In this section, we combine the previous challenges and scale them up: we investigate a ResNet50 classifier [16] trained on CUB-200-2011 [45]. This poses a discriminative space, non-linear component dependencies of varying strengths across multiple variables, and a large 512-dimensional embedding space. One restriction is that CUB has no data-generating components to compare against, so we cannot report DCI scores. However, we qualitatively show that DA can deliver interpretable components in this large-scale setup by matching them to annotated attributes of CUB.

To this end, we applied DA to discover  $K=30$  components of which three are shown exemplarily in Fig. 4. The images with the highest positive scores on the first component (on the right) consistently show white birds. The other end of the component comprises birds whose primary color is black. This gives a high Spearman rank correlation with the CUB attribute “primary color: white”. The other two components are similarly interpretable. We provide an initial quantitative evaluation in Appendix D.5, which indicates that ICA and PCA have problems providing such components. While the construction of further quantitative evaluation schemes goes beyond the scope of this work, these promising results show that DA is applicable to high-dimensional, real-world datasets.

## 6 Discussion and conclusion

Our work constructs a bridge between disentanglement, ICA, and conceptual explanations. We conclude by discussing the implications of our results on these domains, as well as our limitations.

**Implications for disentanglement during training.** Our method searches for linearly embedded concepts in post-hoc and thus depends on the given encoder’s ability to fulfill  $f \circ g = D$ . Experimentally, DA’s DCI score thus rose and fell in sync with its given encoder’s DCI. However, note that this assumption was neither used in the transfer lemma nor in Corollaries 3.1 and 3.2. Thus, if we have access to the encoder during training, e.g., in disentanglement learning, we may regularize it according to DA or OA directly, thus making the  $f \circ g = D$  assumption redundant. In this light, our



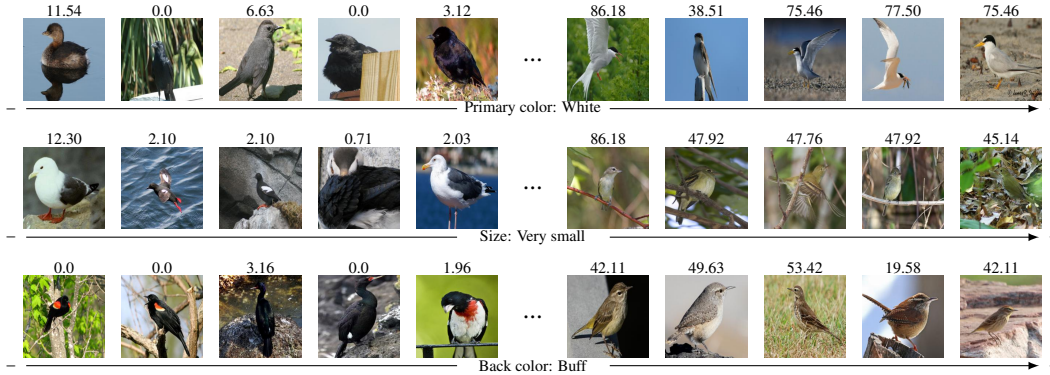


Figure 4: Three exemplary components that DA discovered on CUB, along with images that score the highest (right) and lowest (left) on them. Each component correlates with an interpretable attribute. The numbers on top give the ground-truth value of these attributes provided in CUB.

identifiability result under disjoint Jacobians becomes relevant to the recent branch of literature pursuing orthogonality of  $J_g$ 's columns, both directly [15, 46, 34] and indirectly [35, 29].

**An ICA perspective and a perspective for ICA.** From an ICA perspective, we have a linear mixture  $m : \mathcal{Z} \rightarrow \mathcal{E}$  with  $m = f \circ g$ . The key modification over traditional ICA is that the mixture comprises a decoder and an encoder and that they have traces in their Jacobians. This approach might find applications in non-linear ICA: As we allow  $g$  to be an unknown and non-linear function, it may be interpreted as a non-linear mixture function itself. Our results thus motivate de-mixing  $g$  by learning an encoder  $f$  that imitates properties and thus functional traces that the components leave in  $g$ .

**Limitations.** For future work, we want to carefully investigate the condition of linear disentanglement. Empirically, we saw that it works well for single-object contexts, but it may need to be rethought for some more complex cases, e.g., in multi-object scenes and when we face non-linearly encoded components. Furthermore, we look forward to a standardized evaluation procedure for disentanglement on large-scale real-world datasets such as CUB. While we saw qualitatively meaningful results, a precise quantification would allow to better benchmark disentanglement in the wild.

**Conclusion.** We derived DA, an efficient method to find disentangled components in generative (e.g., VAE-based) and discriminative models. We theoretically proved that it identifies disentangled components in a linear entanglement setting, relying on a purely functional, distribution-agnostic principle. Our extensive experiments reveal that DA is applicable to various disentanglement learning and discriminative models and remains relatively unaffected by distributional challenges.

## Acknowledgments

The authors thank Frederik Träuble, Luigi Gresele, and Julius von Kügelgen for insightful discussions during the development of this project. This work was funded by the Deutsche Forschungsgemeinschaft (DFG, German Research Foundation) under Germany's Excellence Strategy – EXC number 2064/1 – Project number 390727645. The authors thank the International Max Planck Research School for Intelligent Systems (IMPRS-IS) for supporting Michael Kirchhof.

## References

- [1] Arjun Akula, Shuai Wang, and Song-Chun Zhu. Cocox: Generating conceptual and counterfactual explanations via fault-lines. In *Proceedings of the AAAI Conference on Artificial Intelligence*, volume 34, pages 2594–2601, 2020.
- [2] Guillaume Alain and Yoshua Bengio. Understanding intermediate layers using linear classifier probes. *arXiv preprint arXiv:1610.01644*, 2016.
- [3] David Bau, Bolei Zhou, Aditya Khosla, Aude Oliva, and Antonio Torralba. Network dissection: Quantifying interpretability of deep visual representations. In *Proceedings of the IEEE conference on computer vision and pattern recognition*, pages 6541–6549, 2017.

- [4] Yoshua Bengio, Aaron Courville, and Pascal Vincent. Representation learning: A review and new perspectives. *IEEE transactions on pattern analysis and machine intelligence*, 35(8):1798–1828, 2013.
- [5] Arianna Bisazza and Clara Tump. The lazy encoder: A fine-grained analysis of the role of morphology in neural machine translation. In *Proceedings of the 2018 Conference on Empirical Methods in Natural Language Processing*, pages 2871–2876. Association for Computational Linguistics, 2018.
- [6] Peter Blomgren and Tony F Chan. Color tv: total variation methods for restoration of vector-valued images. *IEEE transactions on image processing*, 7(3):304–309, 1998.
- [7] Chris Burgess and Hyunjik Kim. 3d shapes dataset. <https://github.com/deepmind/3dshapes-dataset/>, 2018.
- [8] Christopher P Burgess, Irina Higgins, Arka Pal, Loic Matthey, Nick Watters, Guillaume Desjardins, and Alexander Lerchner. Understanding disentangling in  $\beta$ -VAE. *arXiv preprint arXiv:1804.03599*, 2018.
- [9] Ricky TQ Chen, Xuechen Li, Roger B Grosse, and David K Duvenaud. Isolating sources of disentanglement in variational autoencoders. *Advances in neural information processing systems*, 31, 2018.
- [10] Pierre Comon. Independent component analysis, a new concept? *Signal processing*, 36(3):287–314, 1994.
- [11] Cian Eastwood and Christopher KI Williams. A framework for the quantitative evaluation of disentangled representations. In *International Conference on Learning Representations*, 2018.
- [12] Amirata Ghorbani, James Wexler, James Y Zou, and Been Kim. Towards automatic concept-based explanations. In *Advances in Neural Information Processing Systems*, volume 32, pages 9277–9286, 2019.
- [13] Muhammad Waleed Gondal, Manuel Wuthrich, Djordje Miladinovic, Francesco Locatello, Martin Breidt, Valentin Volchkov, Joel Akpo, Olivier Bachem, Bernhard Schölkopf, and Stefan Bauer. On the transfer of inductive bias from simulation to the real world: a new disentanglement dataset. *Advances in Neural Information Processing Systems*, 32, 2019.
- [14] Ian Goodfellow, Jean Pouget-Abadie, Mehdi Mirza, Bing Xu, David Warde-Farley, Sherjil Ozair, Aaron Courville, and Yoshua Bengio. Generative adversarial nets. *Advances in neural information processing systems*, 27, 2014.
- [15] Luigi Gresele, Julius von Kügelgen, Vincent Stimper, Bernhard Schölkopf, and Michel Besserve. Independent mechanism analysis, a new concept? In *Advances in Neural Information Processing Systems*, 2021.
- [16] Kaiming He, Xiangyu Zhang, Shaoqing Ren, and Jian Sun. Deep residual learning for image recognition. In *Proceedings of the IEEE conference on computer vision and pattern recognition*, pages 770–778, 2016.
- [17] Irina Higgins, Loic Matthey, Arka Pal, Christopher Burgess, Xavier Glorot, Matthew Botvinick, Shakir Mohamed, and Alexander Lerchner. beta-vae: Learning basic visual concepts with a constrained variational framework. In *International Conference on Learning Representations*, 2017.
- [18] Daniella Horan, Eitan Richardson, and Yair Weiss. When is unsupervised disentanglement possible? In *Advances in Neural Information Processing Systems*, 2021.
- [19] Aapo Hyvärinen, Juha Karhunen, and Erkki Oja. *Independent component Analysis*. John Wiley & Sons, Inc, 2001.
- [20] Aapo Hyvärinen and Petteri Pajunen. Nonlinear independent component analysis: Existence and uniqueness results. *Neural Networks*, 12(3):429–439, 1999.
- [21] Aapo Hyvärinen, Hiroaki Sasaki, and Richard Turner. Nonlinear ica using auxiliary variables and generalized contrastive learning. In *The 22nd International Conference on Artificial Intelligence and Statistics*, pages 859–868. PMLR, 2019.
- [22] Dmitry Kazhdan, Botty Dimanov, Mateja Jamnik, Pietro Liò, and Adrian Weller. Now you see me (cme): concept-based model extraction. *AIMLAI workshop at the 29th ACM International Conference on Information and Knowledge Management (CIKM)*, 2020.
- [23] Dmitry Kazhdan, Botty Dimanov, Helena Andres Terre, Mateja Jamnik, Pietro Liò, and Adrian Weller. Is disentanglement all you need? comparing concept-based & disentanglement approaches. *RAI, WeaSul, and RobustML workshops at The Ninth International Conference on Learning Representations 2021*, 2021.
- [24] Ilyes Khemakhem, Diederik Kingma, Ricardo Monti, and Aapo Hyvärinen. Variational autoencoders and nonlinear ICA: A unifying framework. In *International Conference on Artificial Intelligence and Statistics*, pages 2207–2217. PMLR, 2020.
- [25] Been Kim, Martin Wattenberg, Justin Gilmer, Carrie Cai, James Wexler, Fernanda Viegas, et al. Interpretability beyond feature attribution: Quantitative testing with concept activation vectors (tcav). In *International Conference on Machine Learning*, pages 2668–2677. PMLR, 2018.

- [26] Hyunjik Kim and Andriy Mnih. Disentangling by factorising. In *International Conference on Machine Learning*, pages 2649–2658. PMLR, 2018.
- [27] Diederik P Kingma and Max Welling. Auto-encoding variational bayes. *arXiv preprint arXiv:1312.6114*, 2013.
- [28] Pang Wei Koh, Thao Nguyen, Yew Siang Tang, Stephen Mussmann, Emma Pierson, Been Kim, and Percy Liang. Concept bottleneck models. In *International Conference on Machine Learning*, pages 5338–5348. PMLR, 2020.
- [29] Abhishek Kumar and Ben Poole. On implicit regularization in  $\beta$ -vae. In *International Conference on Machine Learning*, pages 5480–5490. PMLR, 2020.
- [30] Abhishek Kumar, Prasanna Sattigeri, and Avinash Balakrishnan. Variational inference of disentangled latent concepts from unlabeled observations. In *International Conference on Learning Representations*, 2018.
- [31] Tobias Leemann, Yao Rong, Stefan Kraft, Enkelejda Kasneci, and Gjergji Kasneci. Coherence evaluation of visual concepts with objects and language. In *ICLR2022 Workshop on the Elements of Reasoning: Objects, Structure and Causality*, 2022.
- [32] Francesco Locatello, Stefan Bauer, Mario Lucic, Gunnar Raetsch, Sylvain Gelly, Bernhard Schölkopf, and Olivier Bachem. Challenging common assumptions in the unsupervised learning of disentangled representations. In *International Conference on Machine Learning*, pages 4114–4124. PMLR, 2019.
- [33] Francesco Locatello, Ben Poole, Gunnar Rätsch, Bernhard Schölkopf, Olivier Bachem, and Michael Tschannen. Weakly-supervised disentanglement without compromises. In *International Conference on Machine Learning*, pages 6348–6359. PMLR, 2020.
- [34] Aditya Ramesh, Youngduck Choi, and Yann LeCun. A spectral regularizer for unsupervised disentanglement. *arXiv preprint arXiv:1812.01161*, 2018.
- [35] Michal Rolínek, Dominik Zietlow, and Georg Martius. Variational autoencoders pursue pca directions (by accident). In *Proceedings of the IEEE/CVF Conference on Computer Vision and Pattern Recognition*, pages 12406–12415, 2019.
- [36] Leonid I Rudin, Stanley Osher, and Emad Fatemi. Nonlinear total variation based noise removal algorithms. *Physica D: nonlinear phenomena*, 60(1-4):259–268, 1992.
- [37] Anna Sepiarskaia, Julia Kiseleva, Maarten de Rijke, et al. Evaluating disentangled representations. *arXiv preprint arXiv:1910.05587*, 2019.
- [38] Harshay Shah, Prateek Jain, and Praneeth Netrapalli. Do input gradients highlight discriminative features? In M. Ranzato, A. Beygelzimer, Y. Dauphin, P.S. Liang, and J. Wortman Vaughan, editors, *Advances in Neural Information Processing Systems*, volume 34, pages 2046–2059, 2021.
- [39] Karen Simonyan, Andrea Vedaldi, and Andrew Zisserman. Deep inside convolutional networks: Visualising image classification models and saliency maps. *arXiv preprint arXiv:1312.6034*, 2013.
- [40] Daniel Smilkov, Nikhil Thorat, Been Kim, Fernanda Viégas, and Martin Wattenberg. Smoothgrad: removing noise by adding noise. In *Workshop on Visualization for Deep Learning, ICML, 2017*.
- [41] Mukund Sundararajan, Ankur Taly, and Qiqi Yan. Axiomatic attribution for deep networks. In *International Conference on Machine Learning*, pages 3319–3328. PMLR, 2017.
- [42] Christian Szegedy, Wojciech Zaremba, Ilya Sutskever, Joan Bruna, Dumitru Erhan, Ian Goodfellow, and Rob Fergus. Intriguing properties of neural networks. *arXiv preprint arXiv:1312.6199*, 2013.
- [43] Frederik Träuble, Elliot Creager, Niki Kilbertus, Francesco Locatello, Andrea Dittadi, Anirudh Goyal, Bernhard Schölkopf, and Stefan Bauer. On disentangled representations learned from correlated data. In *International Conference on Machine Learning*, pages 10401–10412. PMLR, 2021.
- [44] Andrey Voynov and Artem Babenko. Unsupervised discovery of interpretable directions in the gan latent space. In *International Conference on Machine Learning*, pages 9786–9796. PMLR, 2020.
- [45] C. Wah, S. Branson, P. Welinder, P. Perona, and S. Belongie. The Caltech-UCSD Birds-200-2011 Dataset. Technical Report CNS-TR-2011-001, 2011.
- [46] Yuxiang Wei, Yupeng Shi, Xiao Liu, Zhilong Ji, Yuan Gao, Zhongqin Wu, and Wangmeng Zuo. Orthogonal jacobian regularization for unsupervised disentanglement in image generation. In *Proceedings of the IEEE/CVF International Conference on Computer Vision*, pages 6721–6730, 2021.
- [47] Chih-Kuan Yeh, Been Kim, Sercan O Arik, Chun-Liang Li, Tomas Pfister, and Pradeep Ravikumar. On completeness-aware concept-based explanations in deep neural networks. In *Advances in Neural Information Processing Systems*, volume 32, 2019.
- [48] Yujia Zheng, Ignavier Ng, and Kun Zhang. On the identifiability of nonlinear ICA with unconditional priors. In *ICLR2022 Workshop on the Elements of Reasoning: Objects, Structure and Causality*, 2022.

## A Additional Related Work

**Orthogonality constraints for generative models.** In the context of generative adversarial networks (GANs) [14], the problem of analyzing directions has been studied recently [44]. Wen et al. [46] have proposed an orthogonality regularization of the Jacobian, which resulted in more interpretable generative abilities. Ramesh et al. [34] constrain the right-singular vectors of a generator Jacobian to be unit directions, which corresponds to column-wise orthogonal generator Jacobians. We go beyond these works, by providing rigorous results on identifiability and by extending the scope to a much broader class of models.

## B Proofs

### B.1 Transfer lemma

Let  $z \in \mathcal{Z}$  be arbitrary. Since  $(f^* \circ g)(z) = PSz$ , it must be that  $J_{f^*}(g(z))J_g(z) = PS$ .

Now, let us write  $J_{f^*}(g(z)) = [v_1, \dots, v_K]^\top$  with  $v_i \in \mathbb{R}^L$ . Similarly, we can write  $J_g(z) = [w_1, \dots, w_K]$  with  $w_i \in \mathbb{R}^L$ ,  $i = 1, \dots, K$ , and  $S = \text{diag}(\alpha_1, \dots, \alpha_K)$  with  $\alpha_k \in \mathbb{R}_{\neq 0}$ ,  $k = 1, \dots, K$ .

Let us focus on an individual row of  $J_{f^*}$ , i.e., let  $k \in \{1, \dots, K\}$  be a fixed index of a row. Since  $J_{f^*}(z)J_g(z) = PS$  and  $P$  is a permutation matrix with exactly one 1 per row, there is precisely one column index  $k'$  such that the  $k$ -th row and  $k'$ -th column of  $PS$  is non-zero. This setup allows drawing certain conclusions about the vector  $v_k$ . Let  $j = 1, \dots, K$  denote an arbitrary column of  $PS$ . Then,

(i) if  $j = k'$ , then  $v_k^\top w_{k'} = \alpha_{k'} \neq 0$ . In consequence,  $v_k \neq 0$ ,  $w_{k'} \neq 0$  and so we can decompose  $v_k = a_k + b_k$ , where  $a_k \in \text{span}(\{w_{k'}\}) \setminus \{0\}$  and  $b_k \in \text{span}(\{w_{k'}\})^\perp$ , where  $^\perp$  denotes the orthogonal complement. Because  $\text{span}(\{w_{k'}\}) = \{\mu w_{k'} \mid \mu \in \mathbb{R}\}$ , we know that  $a_k = \frac{\alpha_{k'}}{\|w_{k'}\|_2} w_{k'}$ .

(ii) if  $j \neq k'$ , then  $v_k^\top w_j = 0$ . With (i), it follows that  $b_k \in \text{span}(\{w_1, \dots, w_K\})^\perp = \ker(J_g^\top(z))$ .

So, we know that each row of  $J_{f^*}$  must correspond to a (scaled) column of  $J_g$ , plus possibly an element of the kernel of the columns of  $J_g$ . What is left to prove is that this kernel element is zero due to the min TV property, i.e.,  $b_k = 0$ .

The principle of total variation for vector-valued function that  $f^*$  fulfills states (point-wisely evaluated) that  $\|J_{f^*}\|_F$  should be minimal.  $\sqrt{\|J_{f^*}\|_F^2} = \sqrt{\sum_{k=1}^K \|a_k + b_k\|_2^2} = \sqrt{\sum_{k=1}^K \|a_k\|_2^2 + \|b_k\|_2^2}$ , due to the orthogonality of  $a_k$  and  $b_k$ . The unique solution for minimizing this expression that maintains  $f^* \circ g = PS$  (that means fulfilling (i) and (ii)) is  $b_k = 0$ ,  $\forall k = 1, \dots, K$ . Hence,  $v_k = a_k + 0 = \frac{\alpha_{k'}}{\|w_{k'}\|_2} w_{k'} + 0$  for our selected row  $k$ . Globally, this means  $J_{f^*}(g(z)) = P'S'J_g(z)^\top$ , with some scaling matrix  $S'$  and permutation matrix  $P'$ .  $\square$

### B.2 Theorem 1 (non-identifiability)

(1) Since  $f^* = Mf$  is an MDE and  $g$  is IMA, by Corollary 1 we know that  $MJ_f$  must have orthogonal rows. Thus, we can write  $(MJ_f)(MJ_f)^\top = S^*$ , where  $S^* \in \mathbb{R}^{K \times K}$  is a diagonal matrix.

(2) Now, we will show that  $H$  must be a rotated and scaled variant of  $M$ , i.e., it must be  $H = RSM$ , where  $R$  denotes an orthogonal rotation and  $S$  denotes a diagonal scaling matrix.

Since  $M$  and  $H$  have full rank, there exist exactly one pair of a scaling matrix  $S$  and a matrix with normalized rows  $E$  such that  $H = SEM$ .

Suppose for contradiction that some rows of  $E$  were not orthogonal.

Now,  $(HJ_f)(HJ_f)^\top = (SEMJ_f)(SEMJ_f)^\top = SE(MJ_f)(MJ_f)^\top E^\top S^\top = SES^*E^\top S$ . Thus, if two rows of  $E$  were not orthogonal, the corresponding off-diagonal entry of the above expression would be non-zero, and thus  $HJ_f$  could not be orthogonal, contradicting the assumption. Thus,  $E$  must have orthogonal rows and we can write  $H = RSM$ .

(3) Further, it is apparent that any other rotation and scale  $S'R'$  would maintain the orthogonal rows condition of  $H'J_f$  with  $H' = S'R'M$ , while it would not be an MDE anymore since  $S'R'Mf \circ g = S'R'PS = R''S''$ , where  $S''$  is a diagonal scaling and  $R''$  is a rotation – and crucially, not just a permutation – matrix.

In summary, (1) shows that  $H$  identifies the MDE up to rotation and scale, but (2) shows that it does not identify it up to permutation and scale, which is required for an MDE.  $\square$

### B.3 Theorem 2 (identifiability)

(1) We start similar to the proof of the previous theorem. Since  $Mf$  is an MDE and  $g$  is DMA, we can follow via Corrolary 2 that  $MJ_f$  must have disjoint rows.

(2) Now, we will show that  $H$  must be a permuted and scaled variant of  $M$ , i.e., it must be  $H = PSM$ , where  $P$  denotes a permutation and  $S$  denotes a diagonal scaling matrix.

Since  $M$  and  $H$  have full rank, there exist exactly one pair of a scaling matrix  $S$  and a matrix with normalized rows  $E$  such that  $H = SEM$ .

*Suppose for contradiction* that  $E$  was not just a permutation matrix. This means that without loss of generality, that the first row must contain at least two columns that are not equal to zero.

Since  $E$  has full rank, there must be a second row with a non-zero entry in at least one of the columns. Since  $MJ_f$  has disjoint rows,  $EMJ_f$  and thus  $SEMJ_f = HJ_f$  can no longer have disjoint rows. This contradicts the assumption. Hence, it must be  $H = P'S'M$ . Thus,  $Hf \circ g = P'S'Mf \circ g = P'S'PS = P''S''$ , where  $P''$  is a permutation and  $S''$  is a diagonal scaling matrix.  $Hf$  also fulfills the min TV criterion, because it is a linear transform of the min TV encoder  $Mf$ . Thus,  $Hf$  is an MDE.  $\square$

### B.4 IG and SG attributions are homogeneous

**Integrated Gradients.** The Integrated Gradient (IG) attributions for an single model input dimension (e.g., pixel)  $i$  are defined as the integral of the gradients over the path from the input  $x$  to some user-defined baseline  $x'$  for a trained model  $F : \mathbb{R}^L \rightarrow \mathbb{R}$  [41]:

$$\text{IG}_i(F, x) := (x_i - x'_i) \int_{\alpha=0}^1 \frac{\partial F(x' + \alpha(x - x'))}{\partial x_i}. \quad (4)$$

With the trained encoder  $f : \mathbb{R}^L \rightarrow \mathbb{R}^K$ , we compute a different attribution for each output dimension  $j = 1, \dots, K$ . Let  $h \in \mathbb{R}^K$ , we define  $h^\top f(x) := \sum_{j=1}^K h_j f_j(x)$  and obtain the Integrated Gradients

$$\text{IG}_i(h^\top f, x) = (x_i - x'_i) \int_{\alpha=0}^1 \frac{\partial h^\top f(x' + \alpha(x - x'))}{\partial x_i} \quad (5)$$

$$= (x_i - x'_i) \int_{\alpha=0}^1 \sum_{j=1}^K h_j \frac{\partial f_j(x' + \alpha(x - x'))}{\partial x_i} \quad (6)$$

$$= \sum_{j=1}^K h_j (x_i - x'_i) \int_{\alpha=0}^1 \frac{\partial f_j(x' + \alpha(x - x'))}{\partial x_i} \quad (7)$$

$$= \sum_{j=1}^K h_j \text{IG}_i(f_j, x) = h^\top \text{IG}_i(f, x), \quad (8)$$

where  $\text{IG}_i(f, x) \in \mathbb{R}^K$  is a column vector with the attributions for each latent dimension. Applying the above for each row of a matrix  $H \in \mathbb{R}^{R \times K}$ , we arrive at

$$\text{IG}_i(Hf, x) = H \text{IG}_i(f, x). \quad (9)$$

$\square$

**Smoothed Gradients.** Smoothed Gradients (SG) were proposed to mitigate noise in plain gradient attributions. They add noise around the input  $x$ . For the trained model  $F : \mathbb{L}^n \rightarrow \mathbb{R}$  as follows [40]:

$$\text{SG}_i(F, x) := \mathbb{E}_{\epsilon \sim \mathcal{N}(0, \sigma^2)} \left[ \frac{\partial F(x + \epsilon)}{\partial x_i} \right]. \quad (10)$$

Multiplying with a vector  $h \in \mathbb{R}^K$  as before, we obtain

$$\text{SG}_i(h^\top f, x) = \mathbb{E}_{\epsilon \sim \mathcal{N}(0, \sigma^2)} \left[ \frac{\partial h^\top f(x + \epsilon)}{\partial x_i} \right] \quad (11)$$

$$= \mathbb{E}_{\epsilon \sim \mathcal{N}(0, \sigma^2)} \left[ \sum_{j=1}^K h_j \frac{\partial f_j(x + \epsilon)}{\partial x_i} \right] \quad (12)$$

$$= \sum_{j=1}^K h_j \mathbb{E}_{\epsilon \sim \mathcal{N}(0, \sigma^2)} \left[ \frac{\partial f_j(x + \epsilon)}{\partial x_i} \right] = h^\top \text{SG}_i(f, x). \quad (13)$$

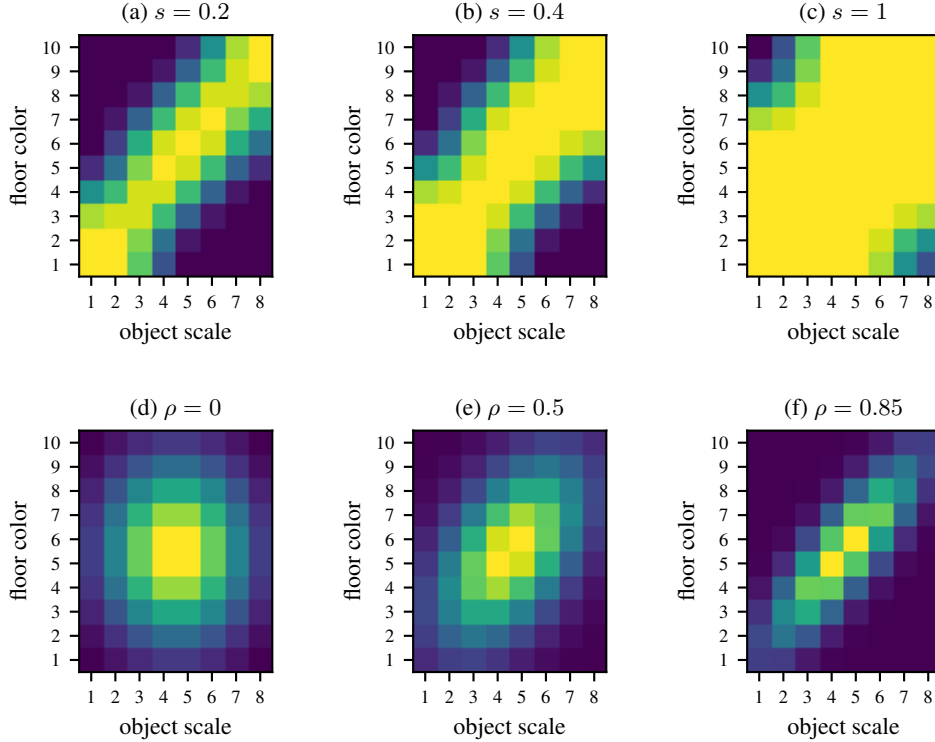


Figure 5: Exemplary correlated densities of the components floor color and object scale under the correlated sampling setup of [15] (a – c) and with our Gaussian sampling (d – f). The correlation strength is indicated on top. Purple denotes a low and yellow a high density.

We can apply this equality for rows of the matrix  $H \in \mathbb{R}^{R \times K}$  again which analogously yields

$$\text{SG}_i(Hf, x) = H\text{SG}_i(f, x). \quad (14)$$

□

**Remark:** Note that if this relation holds for attributions of a single pixel  $i$ , it will also hold for the  $\mathbb{R}^{K \times L}$  attribution matrix  $\mathcal{A}(f, x) = [\text{SG}_1(f, x), \dots, \text{SG}_L(f, x)]$ , i.e.,  $\mathcal{A}(Hf, x) = H\mathcal{A}(f, x)$ .

## C Experimental Details

### C.1 Architectures

For the disentanglement models, we use the implementations provided by the open source library `disentanglement-pytorch`<sup>2</sup>. For the evaluation measures, we use the implementation of `disentanglement_lib`<sup>3</sup> with their respective default parameters. We use a simple encoder and decoder architecture, that consists of five and six feed-forward convolutional layers respectively and relies on the ReLU activation function.

### C.2 Correlated sampling

In this paper, we use two methods to introduce correlations between the ground truth components. Both methods rely on proportional resampling: We first draw a batch that has multiple times the final batch size (we use factors from 3-6 depending on the non-uniformity of the distribution), then compute the (unnormalized) probability of each sample under a given distribution over the component values, and then resample a final batch (with replacement) proportional to these probabilities.

<sup>2</sup><https://github.com/amir-abdi/disentanglement-pytorch>

<sup>3</sup>[https://github.com/google-research/disentanglement\\_lib](https://github.com/google-research/disentanglement_lib)

The two methods differ in the probability distribution assigned to the component values. The first setting (used in Sec. 5.2) uses the approach of [43]: As visualized in Fig. 5(a) to (c), we pick two components  $z_1$  and  $z_2$ , create the grid of possible values, and then lay a diagonal line over this grid. Along this line, we set a normal distribution with a standard deviation  $s$ . A higher  $s$  means that the distribution gives a higher probability to more component combinations of the grid, whereas a smaller  $s$  is more restrictive. Mathematically, it is defined by [43] as:

$$p(z_1, z_2) \propto \exp\left(-\frac{(z_1 - \alpha z_2)^2}{2s^2}\right), \quad (15)$$

where  $\alpha = z_1^{\max}/z_2^{\max}$  brings the components to a same scale and  $s$  is similarly normalized to the maximum values that  $z_1$  and  $z_2$  can take. The remaining components  $z_i, i > 2$ , are marginalized out of this distribution and thus continue to be sampled uniformly at random.

This setting is limited to one pair of components and also introduces a non-Gaussian distribution over all components. To tackle these limitations and thus to make the distributional challenge harder, we use a different probability distribution in Sec. 5.3. Here, we lay a normal distribution over *all* components, i.e.,  $z \sim \mathcal{N}(\mu, \Sigma)$ , where  $\mu$  is centered in the middle of the possible values, i.e.,  $\mu = \frac{z^{\max} - z^{\min}}{2}$ .  $\Sigma$  is similarly normalized, since we decompose it into  $\Sigma = \text{diag}(\sigma^2)\Gamma$ .

The vector  $\sigma \in \mathbb{R}_{>0}^K$  gives standard deviations for each component via  $\sigma^2 = \left(\frac{\mu+0.5}{2}\right)^2$  such that the distribution stretches across the grid of possible values. Note that the +0.5 is because the values are assumed to be zero-indexed.  $\Gamma$  is a correlation matrix with 1 on its diagonal. In the first experiment in Sec. 5.3, we correlate only one pair of variables and set their corresponding off-diagonal entries in  $\Gamma$  to  $\rho$ . Fig. 5 (d) to (f) show the corresponding marginal distributions of these components. In the second experiment, we fill  $\Gamma$  with several correlations in the following order:

$$\begin{matrix} z_1 \\ z_2 \\ z_3 \\ z_4 \\ z_5 \\ z_6 \end{matrix} \begin{pmatrix} 1 & 4 & 12 & 14 & 9 & \\ & 11 & 5 & 10 & 6 & \\ & & 3 & 8 & 15 & \\ & & & 13 & 7 & \\ & & & & 2 & \\ & & & & & \end{pmatrix} \quad (16)$$

where the component order of the rows and columns is  $z_1 = \text{floor\_color}$ ,  $z_2 = \text{background\_color}$ ,  $z_3 = \text{object\_color}$ ,  $z_4 = \text{object\_scale}$ ,  $z_5 = \text{object\_shape}$ ,  $z_6 = \text{orientation}$ . Here, it is important to ascertain that the covariance matrix stays positive definite. Thus, we start with  $\rho = 0.7$ , check if the lowest eigenvalue of  $\Sigma$  is at least 0.2, and if not, reduce  $\rho$  by a factor of 0.9 until the eigenvalue fulfills this property. While technically it would be enough to have the smallest eigenvalue anywhere above 0, we found that 0.2 helps in numerical stability, for instance when inverting the covariance matrix to compute the multivariate normal distribution density.

### C.3 Discriminative setup

The decision tree that is used to generate the class distribution is shown in Figure 6. It relies on 4 (binarized) components. We trained a simple CNN classifier for this problem using the cross-entropy loss. In addition to the classification loss terms, we add a regularizer  $\|z\|_2^2$ , which constrains the latent codes to not grow arbitrarily large, during training. To create a realistic setup, we subsample the dataset to follow a normal distribution as shown in Fig. 5d. We also add label noise near the decision boundary: For objects which have an orientation that is nearly centered, we follow each branch (left/right) with a probability of 50%. With increasing left-orientedness, the probability of following the left branch increases to almost 100% in form of a sigmoid function over the actual orientation. We follow the same procedure for the remaining features. We train the classifier for 10k iterations at a batch size of 24 and verify that it reaches an accuracy close to the best-possible one taking the mislabeled samples into account. We add correlations by increasing the chance of the the factors *obj. color* and *floor color* taking the same binary value. We use our disjoint attributions approach to find a  $H \in \mathbb{R}^{4 \times 6}$  matrix that should map the 6-dimensional latent space of the model to the four binary concepts that are used in the classification task. For the unit directions, we take the first four unit directions of the latent space, for PCA and ICA, we take the most prominent for components discovered for the evaluation with the four annotated ground truth concepts.

### C.4 Evaluation scores

Several scores to quantify disentanglement have been proposed in the literature and often emphasize a different aspect of disentanglement [37]. Among the most common scores are the DCI [11], MIG [9], SAP [30] and the FactorVAE metric [26]. However, it is unclear which of these metrics (or if any) also provide useful results in the correlated setting [43]. Therefore, to compute the reliable evaluations, we train the model (and the post-processing methods such

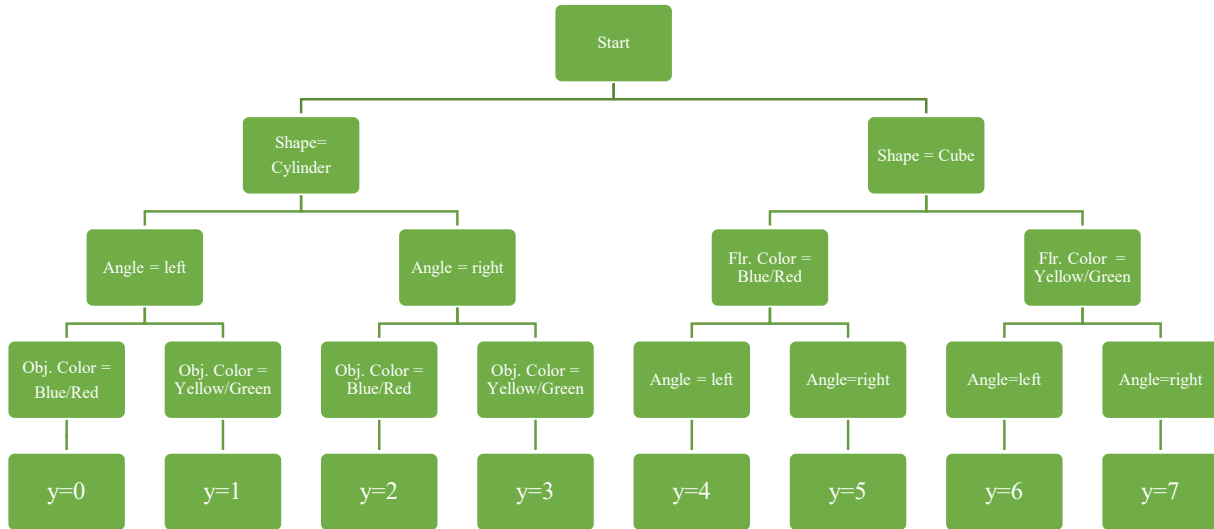


Figure 6: The decision tree setup that we use for the discriminative classification problem. Each image is assigned one out of eight class labels  $y$  according to the following decision tree.

as PCA, ICA, OA, DA) on the correlated dataset, but compute the metrics on samples from the full, *uncorrelated* datasets to avoid distortion in our scores. Träuble et al. noted that the DCI scores were able to discover entanglement between 2 variables [43, Figure 11, Appendix], whereas most other metrics failed even in this case. Therefore, we mainly rely on this score for our experiments but also report results for the other scores in Experiment Sec. 5.2 that show a similar picture in this appendix (Appendix D.3).

## C.5 CUB experiments

CUB-200-2011 is a fine-grained dataset containing a total of 11,788 images of 200 bird species (5994 for training and 5794 for testing). We trained a ResNet-50 with two fully-connected (fc) layers (the second fc layer served as a bottleneck layer and took 2048-dim feature vectors as input and output 512-dim ones) on CUB for 100 epochs using a SGD optimizer with an initial learning rate of 0.001. The input images were center cropped to  $224 \times 224$  pixels. Trained on a standard cross-entropy loss, the ResNet achieved a classification accuracy of on average 77.47% on five random seeds, indicating proper training. After training the classifier, we applied our proposed method to discover components in the embedding space.

CUB provides no ground-truth components since it is a real-world dataset. It does, however, contain 312 attributes semantically describing the bird classes, e.g., wing color or beak shape. These attributes have no guarantee to be complete, but they offer 312 interpretable components. This allows for an attempt to quantify whether our discovered components are interpretable and meaningful by comparing whether they match some of these interpretable ones.

Formally, we are given a set of image feature embeddings  $\{e_n\}_{n=1,\dots,N}$ ,  $e_n \in \mathbb{R}^L$  and a found matrix  $H = (h_1, \dots, h_K) \in \mathbb{R}^{L \times K}$  that contains the directions of discovered components ( $L = 512$ ,  $K = 30$ ). A score  $s_n^k$  of  $n$ -th image for the  $k$ -th discovered component can be calculated by projecting the feature embeddings on that component direction, i.e.,  $s_n^k = \langle e_n, h_k \rangle$ . One pitfall is that  $s_n^k$  can be negative, indicating, e.g., a non-black bird for the component "primary color: black", but this opposite attribute is usually encoded in a separate attribute in CUB, e.g., "primary color: white". Thus, we separate the negative and positive values into two components, resulting in  $2 \cdot K$  positive scores for each image.

To compare these component scores with the attributes, we make use of the numerical attribute values provided in CUB. First, we average the  $2 \cdot K$  component values of all images of a class, to be comparable with the class-wise attributes provided by CUB. This gives us a numerical  $2 \cdot K$  dimensional component description and a 312 dimensional attribute description per class. Now, we match the discovered components to the attributes. We compare each discovered component to each attributes via the Spearman's rank correlation coefficient and consider the attribute with the highest score to match the component. These are the matches used in Sec. 5.5. We further use the (average) Spear-



Model	Ranges
BetaVAE	$\beta \in \{1, 2, 4, 6, 8, 16\}$
FactorVAE	$\gamma \in \{5, 8, 10, 20, 30, 40, 50, 100\}$
BetaTCVAE	$\beta \in \{1, 2, 4, 6, 8, 10\}$
DIPVAEI	$\lambda_{od} \in \{1, 2, 5, 10, 20, 50\}$

Table 3: The hyperparameter ranges considered in this work.

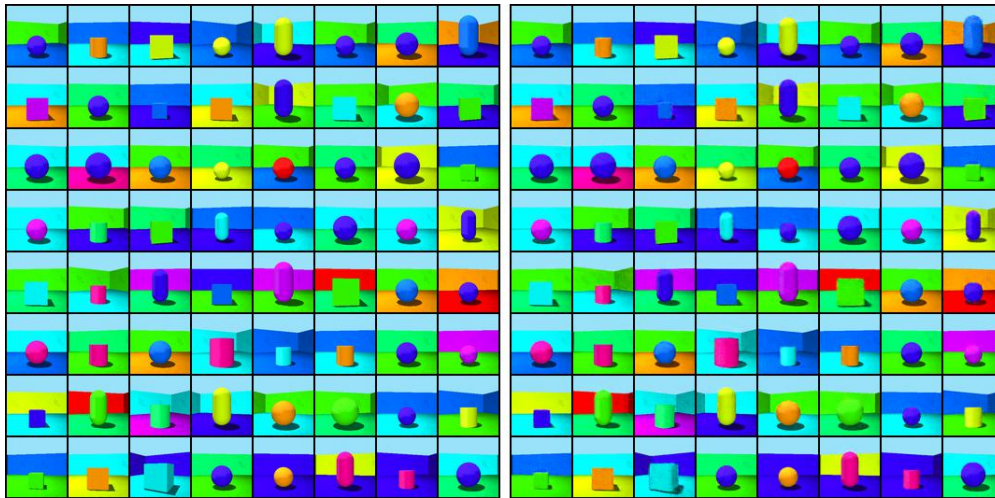


Figure 7: Random example images (left) and their reconstructions (right) of a BetaVAE on Shapes3D.

man’s rank correlation across all components to their best-matching attributes to quantify how well the components match to interpretable attributes in Appendix D.5.

## C.6 Hyperparameters for the disentanglement models

We orient our hyperparameter ranges by the works [43, 32]. The exact ranges are provided in Tab. 3. We find the best hyperparameters in the ranges for each correlation strength/dataset/model triple separately. Then we train five models from independent seeds to run our experiments. We use the Adam optimizer for all model with a learning rate of  $10^{-4}$ , batch size of 64 and train for 300k iterations (equiv. to 40 epochs on Shapes3D).

For the optimization of the post-hoc disentanglement problem, we use slightly different hyperparameters. We use the RMSProp optimizer with learning rate of  $10^{-3}$  and a batch size of 48.

## D Additional results

### D.1 Reconstruction quality

In Sec. 5.2, we saw low disentanglement scores of both the base and post-hoc models on MPI3D-real compared to the performance on Shapes3D. This implies that the embedding spaces of the VAEs was not trained well. In fact, this is supported by the reconstruction quality on both Shapes3D and MPI3D-real. Figures 7 and 8 show the original images on the left and the reconstructions of a randomly chosen BetaVAE on the right. On Shapes3D, the BetaVAE is able to reconstruct the image from its embedding representation. On MPI3D-real, it is able to reconstruct the big image parts shared across many pictures (ground, background stripe and background), but becomes blurry in the smaller and more nuanced robot arm and object shapes. This indicates that the information on these components might not be stored in the embedding space and is thus hardly disentangled. A longer training (800k instead of 300k iterations) did not resolve the issue. The issue might arise, following [13], because the input images were scaled down to 64x64 pixels making the detailed objects hard to perceive, and because the same architecture as in the Shapes3D experiments was used, which might not be expressive enough.

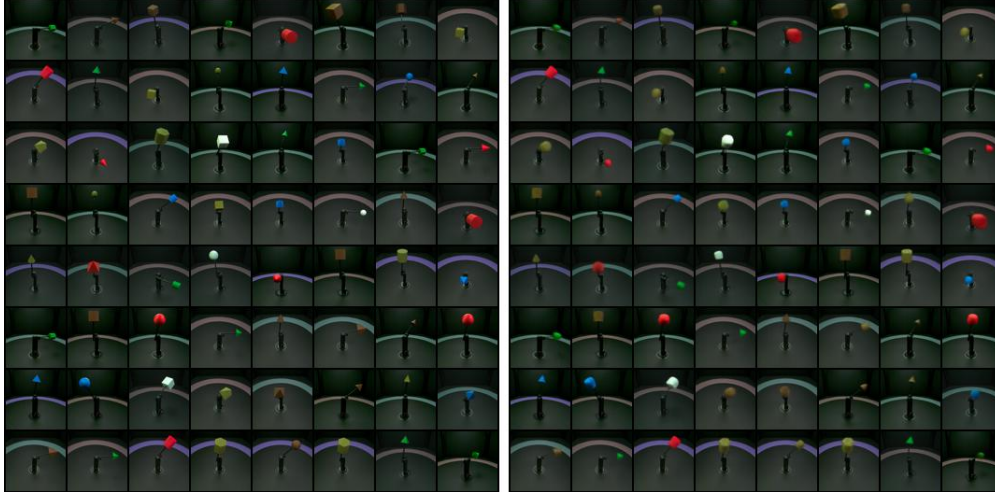


Figure 8: Random example images (left) and their reconstructions (right) of a BetaVAE on MPI3D-real.

Model	BetaVAE			FactorVAE			BetaTCVAE			DIPVAEI		
	$s = 0.2$	$s = 0.4$	$s = \infty$	$s = 0.2$	$s = 0.4$	$s = \infty$	$s = 0.2$	$s = 0.4$	$s = \infty$	$s = 0.2$	$s = 0.4$	$s = \infty$
Correlation	0.666	0.497	0.650	0.441	0.507	0.651	0.580	0.619	0.504	0.686	0.631	0.868
unit dirs.	$\pm 0.030$	$\pm 0.028$	$\pm 0.049$	$\pm 0.065$	$\pm 0.105$	$\pm 0.087$	$\pm 0.022$	$\pm 0.008$	$\pm 0.056$	$\pm 0.072$	$\pm 0.018$	$\pm 0.052$
PCA	0.287	0.263	0.357	0.312	0.358	0.484	0.341	0.400	0.396	0.266	0.158	0.215
	$\pm 0.010$	$\pm 0.028$	$\pm 0.024$	$\pm 0.048$	$\pm 0.075$	$\pm 0.064$	$\pm 0.018$	$\pm 0.030$	$\pm 0.061$	$\pm 0.029$	$\pm 0.013$	$\pm 0.037$
ICA	0.394	0.574	0.674	0.193	0.294	0.390	0.516	0.540	<b>0.642</b>	0.672	0.630	<b>0.870</b>
	$\pm 0.099$	$\pm 0.040$	$\pm 0.012$	$\pm 0.052$	$\pm 0.070$	$\pm 0.109$	$\pm 0.019$	$\pm 0.023$	<b><math>\pm 0.007</math></b>	$\pm 0.073$	$\pm 0.018$	<b><math>\pm 0.049</math></b>
Grad (OA)	0.638	0.617	0.556	0.478	0.551	<b>0.666</b>	0.548	0.623	0.551	0.705	0.644	0.794
	$\pm 0.067$	$\pm 0.018$	$\pm 0.109$	$\pm 0.046$	$\pm 0.040$	<b><math>\pm 0.041</math></b>	$\pm 0.035$	$\pm 0.021$	$\pm 0.038$	$\pm 0.062$	$\pm 0.019$	$\pm 0.043$
IG (OA)	0.702	0.460	0.578	0.470	0.511	0.581	0.619	0.533	0.612	0.650	0.605	0.701
	$\pm 0.035$	$\pm 0.128$	$\pm 0.117$	$\pm 0.035$	$\pm 0.042$	$\pm 0.066$	$\pm 0.024$	$\pm 0.006$	$\pm 0.024$	$\pm 0.072$	$\pm 0.006$	$\pm 0.045$
SG (OA)	0.677	0.438	0.609	0.475	0.561	0.644	0.533	0.620	0.559	0.698	0.642	0.785
	$\pm 0.037$	$\pm 0.127$	$\pm 0.131$	$\pm 0.042$	$\pm 0.040$	$\pm 0.055$	$\pm 0.028$	$\pm 0.021$	$\pm 0.040$	$\pm 0.060$	$\pm 0.017$	$\pm 0.046$
Grad (DA)	0.645	<b>0.641</b>	<b>0.690</b>	0.547	0.584	0.385	<b>0.629</b>	0.666	0.598	<b>0.717</b>	<b>0.684</b>	0.857
	$\pm 0.067$	<b><math>\pm 0.031</math></b>	<b><math>\pm 0.062</math></b>	$\pm 0.056$	$\pm 0.047$	$\pm 0.169$	<b><math>\pm 0.033</math></b>	$\pm 0.010$	$\pm 0.057$	<b><math>\pm 0.059</math></b>	<b><math>\pm 0.009</math></b>	$\pm 0.037$
IG (DA)	0.645	0.530	0.548	<b>0.573</b>	<b>0.615</b>	0.631	0.607	0.624	0.584	0.703	0.659	0.771
	$\pm 0.076$	$\pm 0.106$	$\pm 0.114$	<b><math>\pm 0.046</math></b>	<b><math>\pm 0.045</math></b>	$\pm 0.128$	$\pm 0.028$	$\pm 0.021$	$\pm 0.039$	$\pm 0.073$	$\pm 0.008$	$\pm 0.029$
SG (DA)	<b>0.711</b>	0.593	0.633	0.506	0.600	0.644	0.628	<b>0.670</b>	0.595	0.716	0.682	0.851
	<b><math>\pm 0.040</math></b>	$\pm 0.094$	$\pm 0.062$	$\pm 0.057$	$\pm 0.027$	$\pm 0.066$	$\pm 0.033$	<b><math>\pm 0.014</math></b>	$\pm 0.059$	$\pm 0.059$	$\pm 0.010$	$\pm 0.036$

Table 4: Mean  $\pm$  std. err. of the DCI score of the experiments in Sec. 5.2 for the first correlated component pair (*floor* vs *background* color) in Shapes3D, as an ablation study with further correlations strengths and attribution methods. We observe only small differences between attribution methods, with plain Grad and SG performing best in the DA setting.

## D.2 Correlation strengths and attribution methods in first experiment

In this section we provide additional ablations for the rectification experiment in Sec. 5.2. We investigate the impact of the choice of attribution method and the correlation strength  $s$ . The values (DCI scores) are shown in Tab. 4. As expected, our approach offers the highest gains over the baseline when the correlation is higher. Starting at  $s = 0.4$ , our runs start to reliably outperform the baselines. Regarding the attributions, there is no clear picture, but Grad and SG seem to yield good results more stably across runs. DA usually outperforms OA, which supports our theoretical results on identifiability.

## D.3 Further disentanglement metrics

Tables 5 – 7 show the results of the experiment in Sec. 5.2 measured in the alternative metrics MIG, FactorVAE and SAP score. We use the SG-Variant of our orthogonal attribution loss for the optimization in all plots. For MIG, we

Dataset	Shapes3D			MPI3D-real		
	Correlated factors	floor vs. background	orientation vs. background	orientation vs. size	background vs. object color	background vs. robot arm dof-1
<b>BetaVAE</b>	0.309 ± 0.031	0.426 ± 0.043	0.335 ± 0.059	0.232 ± 0.022	0.185 ± 0.031	<b>0.196 ± 0.034</b>
+PCA	0.111 ± 0.031	0.101 ± 0.009	0.092 ± 0.031	0.095 ± 0.010	0.105 ± 0.023	0.123 ± 0.033
+ICA	0.360 ± 0.040	0.324 ± 0.054	0.277 ± 0.036	0.155 ± 0.025	0.163 ± 0.014	0.071 ± 0.014
+Ours (OA)	0.511 ± 0.029	0.437 ± 0.044	0.502 ± 0.030	<b>0.239 ± 0.021</b>	<b>0.229 ± 0.022</b>	0.187 ± 0.039
+Ours (DA)	<b>0.594 ± 0.023</b>	<b>0.485 ± 0.057</b>	<b>0.545 ± 0.034</b>	0.193 ± 0.036	0.092 ± 0.038	0.080 ± 0.015
<b>FactorVAE</b>	0.297 ± 0.084	0.319 ± 0.076	<b>0.423 ± 0.018</b>	0.079 ± 0.001	0.103 ± 0.020	0.080 ± 0.010
+PCA	0.202 ± 0.057	0.135 ± 0.028	0.235 ± 0.036	<b>0.111 ± 0.006</b>	<b>0.122 ± 0.011</b>	<b>0.107 ± 0.009</b>
+ICA	0.199 ± 0.061	0.106 ± 0.025	0.078 ± 0.021	0.018 ± 0.008	0.061 ± 0.015	0.069 ± 0.015
+Ours (OA)	<b>0.337 ± 0.033</b>	<b>0.322 ± 0.056</b>	0.288 ± 0.092	0.070 ± 0.014	0.086 ± 0.018	0.039 ± 0.014
+Ours (DA)	0.276 ± 0.036	0.217 ± 0.064	0.213 ± 0.036	0.046 ± 0.021	0.045 ± 0.016	0.048 ± 0.015
<b>BetaTCVAE</b>	0.333 ± 0.008	0.400 ± 0.046	0.402 ± 0.017	<b>0.279 ± 0.025</b>	<b>0.223 ± 0.030</b>	0.201 ± 0.039
+PCA	0.249 ± 0.033	0.145 ± 0.039	0.184 ± 0.062	0.265 ± 0.019	0.203 ± 0.028	<b>0.213 ± 0.035</b>
+ICA	0.390 ± 0.031	0.276 ± 0.043	0.346 ± 0.072	0.199 ± 0.040	0.158 ± 0.038	0.170 ± 0.033
+Ours (OA)	0.484 ± 0.025	0.490 ± 0.033	0.526 ± 0.036	0.092 ± 0.029	0.071 ± 0.029	0.041 ± 0.014
+Ours (DA)	<b>0.525 ± 0.014</b>	<b>0.540 ± 0.021</b>	<b>0.620 ± 0.024</b>	0.120 ± 0.037	0.122 ± 0.044	0.075 ± 0.028
<b>DipVAE</b>	0.493 ± 0.032	0.481 ± 0.020	0.433 ± 0.044	0.138 ± 0.020	0.099 ± 0.040	<b>0.143 ± 0.045</b>
+PCA	0.063 ± 0.006	0.086 ± 0.027	0.108 ± 0.014	0.054 ± 0.016	0.042 ± 0.011	0.064 ± 0.010
+ICA	0.495 ± 0.032	0.438 ± 0.053	0.224 ± 0.026	0.138 ± 0.023	0.096 ± 0.040	0.139 ± 0.047
+Ours (OA)	0.512 ± 0.042	0.425 ± 0.036	0.465 ± 0.049	<b>0.146 ± 0.019</b>	<b>0.105 ± 0.033</b>	0.136 ± 0.049
+Ours (DA)	<b>0.591 ± 0.028</b>	<b>0.546 ± 0.017</b>	<b>0.497 ± 0.060</b>	0.133 ± 0.029	0.094 ± 0.036	0.125 ± 0.045

Table 5: Mean ± std. err. of the Mutual-Information Gap (MIG) scores of four post-hoc methods applied to the embedding spaces of four disentanglement models on two datasets with different pairs of correlated variables.

see similar results as for DCI in the main paper. The results in FactorVAE and SAP score are slightly inferior but our approach still improves over the baseline in many setups.

#### D.4 Qualitative results on Shapes3D

In this section, we want to show another traversal plot like the one in Fig. 1 and more thoroughly analyze its latent space. We chose another architecture (BetaTCVAE) and  $s = 0.2$  with the usual correlated factors *floor color* and *background color*. Out of the 5 independent runs, we selected the one with the highest DCI score (of the base model) for the analysis.

**Linear entanglement matrix.** To study which factors are encoded in which latent dimension, we compute a matrix of linear entanglement. By our linear entanglement hypothesis,  $z' = Dz$ , where the matrix  $D = [d_1, \dots, d_k] \in \mathbb{R}^{K \times K}$  contains the directions  $d_i \in \mathbb{R}^K$ , in which the ground truth concepts are encoded. Changing the component  $i$  (entry  $z_i$ ) by one unit will change the resulting embedding by  $d_i$ . To find these  $d_i$ , we take the factors at the origin of the traversal plot and alter only a single component  $i$ . We then encode the image corresponding to that change, and measure the change in embeddings to find the linear direction  $d_i$  that the corresponding component is encoded in (to be precise, we sample several changes and take the largest eigenvector of the embedding changes covariance). Thus, we can estimate the matrix  $D$ . To estimate which factors are changing, when a unit direction of the (plain or postprocessed) embedding space is followed (a change in  $z'_i$ ), we can invert the equation to  $z = D^{-1}z'$ . The columns in  $D^{-1}$  correspond to the change in ground truth components that going one unit in the latent space coordinate  $i$  will entail. We refer to this matrix  $D^{-1}$ , that shows which ground truth components will be altered by moving along one latent dimension as *linear entanglement matrix*.

Figure 9 shows the traversals along with the corresponding linear entanglement matrices that correspond well to the changes observed. For the plain method, the components that were correlated are deeply entangled (upper line). However, our method (DA, SG, lower line) is able to separate them well, which is testified both by the traversal and the linear disentanglement matrix.

Dataset	Shapes3D			MPI3D-real		
	Correlated factors	floor vs. background	orientation vs. background	orientation vs. size	background vs. object color	background vs. robot arm dof-1
<b>BetaVAE</b>	<b>0.834 ± 0.022</b>	<b>0.839 ± 0.053</b>	0.828 ± 0.011	0.557 ± 0.032	0.490 ± 0.044	0.412 ± 0.022
+PCA	0.722 ± 0.060	0.689 ± 0.047	0.716 ± 0.035	0.393 ± 0.037	0.452 ± 0.031	0.398 ± 0.031
+ICA	0.797 ± 0.036	0.775 ± 0.083	0.794 ± 0.022	0.385 ± 0.100	0.262 ± 0.061	0.251 ± 0.031
+Ours (OA)	0.767 ± 0.108	0.808 ± 0.060	<b>0.832 ± 0.022</b>	0.565 ± 0.022	0.504 ± 0.036	0.443 ± 0.027
+Ours (DA)	0.813 ± 0.087	0.829 ± 0.068	0.826 ± 0.029	<b>0.567 ± 0.024</b>	<b>0.525 ± 0.042</b>	<b>0.444 ± 0.027</b>
<b>FactorVAE</b>	0.636 ± 0.045	0.622 ± 0.064	0.595 ± 0.050	<b>0.354 ± 0.016</b>	<b>0.389 ± 0.015</b>	0.342 ± 0.006
+PCA	0.627 ± 0.071	<b>0.680 ± 0.027</b>	<b>0.652 ± 0.024</b>	0.330 ± 0.018	0.388 ± 0.022	<b>0.353 ± 0.016</b>
+ICA	0.619 ± 0.059	0.446 ± 0.146	0.200 ± 0.148	0.277 ± 0.013	0.242 ± 0.082	0.304 ± 0.017
+Ours (OA)	<b>0.663 ± 0.022</b>	0.661 ± 0.028	0.644 ± 0.051	0.347 ± 0.007	0.386 ± 0.020	0.337 ± 0.013
+Ours (DA)	0.646 ± 0.026	0.637 ± 0.023	0.619 ± 0.026	0.330 ± 0.015	0.375 ± 0.016	0.335 ± 0.013
<b>BetaTCVAE</b>	0.676 ± 0.012	0.814 ± 0.052	0.877 ± 0.015	0.445 ± 0.044	0.379 ± 0.021	0.346 ± 0.020
+PCA	0.761 ± 0.035	0.738 ± 0.063	0.794 ± 0.037	<b>0.505 ± 0.040</b>	<b>0.425 ± 0.012</b>	0.389 ± 0.008
+ICA	0.834 ± 0.004	0.761 ± 0.051	0.806 ± 0.051	0.149 ± 0.099	0.168 ± 0.053	0.057 ± 0.035
+Ours (OA)	0.837 ± 0.004	0.849 ± 0.015	<b>0.879 ± 0.013</b>	0.463 ± 0.048	0.401 ± 0.018	0.399 ± 0.019
+Ours (DA)	<b>0.842 ± 0.000</b>	<b>0.854 ± 0.017</b>	0.878 ± 0.013	0.460 ± 0.046	0.399 ± 0.018	<b>0.399 ± 0.014</b>
<b>DipVAE</b>	<b>0.826 ± 0.006</b>	0.839 ± 0.006	0.785 ± 0.033	<b>0.517 ± 0.046</b>	<b>0.473 ± 0.046</b>	0.430 ± 0.013
+PCA	0.671 ± 0.019	0.603 ± 0.064	0.653 ± 0.039	0.431 ± 0.028	0.373 ± 0.027	0.344 ± 0.021
+ICA	0.826 ± 0.006	0.831 ± 0.007	0.749 ± 0.027	0.434 ± 0.042	0.423 ± 0.027	0.424 ± 0.012
+Ours (OA)	0.824 ± 0.007	0.812 ± 0.018	0.785 ± 0.029	0.503 ± 0.044	0.471 ± 0.035	0.436 ± 0.021
+Ours (DA)	0.822 ± 0.006	<b>0.850 ± 0.012</b>	<b>0.809 ± 0.045</b>	0.505 ± 0.040	0.459 ± 0.040	<b>0.448 ± 0.026</b>

Table 6: Mean ± std. err. of the FactorVAE scores of four post-hoc methods applied to the embedding spaces of four disentanglement models on two datasets with different pairs of correlated variables.

Dataset	Shapes3D			MPI3D-real		
	Correlated factors	floor vs. background	orientation vs. background	orientation vs. size	background vs. object color	background vs. robot arm dof-1
<b>BetaVAE</b>	0.086 ± 0.003	0.119 ± 0.004	0.100 ± 0.005	0.127 ± 0.014	0.098 ± 0.015	<b>0.092 ± 0.025</b>
+PCA	0.047 ± 0.005	0.062 ± 0.006	0.066 ± 0.006	0.027 ± 0.005	0.055 ± 0.008	0.037 ± 0.006
+ICA	0.007 ± 0.001	0.013 ± 0.001	0.019 ± 0.004	0.017 ± 0.006	0.007 ± 0.002	0.004 ± 0.001
+Ours (OA)	<b>0.099 ± 0.026</b>	0.114 ± 0.008	0.112 ± 0.007	<b>0.131 ± 0.011</b>	<b>0.113 ± 0.005</b>	0.082 ± 0.024
+Ours (DA)	0.094 ± 0.020	<b>0.127 ± 0.012</b>	<b>0.114 ± 0.013</b>	0.107 ± 0.025	0.059 ± 0.024	0.037 ± 0.013
<b>FactorVAE</b>	0.072 ± 0.006	0.059 ± 0.006	<b>0.064 ± 0.001</b>	0.059 ± 0.004	0.066 ± 0.008	0.054 ± 0.003
+PCA	0.060 ± 0.006	<b>0.066 ± 0.004</b>	0.057 ± 0.004	<b>0.065 ± 0.008</b>	<b>0.076 ± 0.004</b>	<b>0.071 ± 0.003</b>
+ICA	0.013 ± 0.002	0.008 ± 0.001	0.006 ± 0.002	0.002 ± 0.000	0.002 ± 0.001	0.001 ± 0.000
+Ours (OA)	<b>0.077 ± 0.012</b>	0.052 ± 0.005	0.054 ± 0.017	0.054 ± 0.006	0.059 ± 0.006	<b>0.036 ± 0.015</b>
+Ours (DA)	0.071 ± 0.014	0.053 ± 0.012	0.040 ± 0.010	0.041 ± 0.017	0.043 ± 0.015	0.044 ± 0.013
<b>BetaTCVAE</b>	0.052 ± 0.002	0.107 ± 0.013	0.096 ± 0.016	<b>0.151 ± 0.017</b>	<b>0.133 ± 0.007</b>	<b>0.117 ± 0.011</b>
+PCA	0.073 ± 0.004	0.075 ± 0.011	0.107 ± 0.015	0.148 ± 0.018	0.125 ± 0.009	0.109 ± 0.007
+ICA	0.015 ± 0.000	0.010 ± 0.001	0.011 ± 0.002	0.011 ± 0.004	0.005 ± 0.002	0.004 ± 0.002
+Ours (OA)	0.105 ± 0.003	0.119 ± 0.012	<b>0.130 ± 0.023</b>	0.055 ± 0.017	0.059 ± 0.016	0.056 ± 0.003
+Ours (DA)	<b>0.108 ± 0.005</b>	<b>0.127 ± 0.013</b>	0.109 ± 0.017	0.071 ± 0.020	0.072 ± 0.010	0.051 ± 0.015
<b>DipVAE</b>	0.083 ± 0.004	0.084 ± 0.003	0.070 ± 0.002	0.056 ± 0.011	0.039 ± 0.013	0.057 ± 0.016
+PCA	0.027 ± 0.003	0.034 ± 0.006	0.043 ± 0.004	0.023 ± 0.004	0.030 ± 0.008	0.022 ± 0.005
+ICA	0.006 ± 0.001	0.003 ± 0.002	0.030 ± 0.002	0.011 ± 0.005	0.005 ± 0.003	0.005 ± 0.002
+Ours (OA)	0.089 ± 0.012	0.082 ± 0.005	0.077 ± 0.002	<b>0.060 ± 0.008</b>	<b>0.047 ± 0.010</b>	<b>0.061 ± 0.016</b>
+Ours (DA)	<b>0.114 ± 0.003</b>	<b>0.105 ± 0.008</b>	<b>0.084 ± 0.007</b>	0.051 ± 0.008	0.043 ± 0.012	0.054 ± 0.016

Table 7: Mean ± std. err. of the SAP scores of four post-hoc methods applied to the embedding spaces of four disentanglement models on two datasets with different pairs of correlated variables.

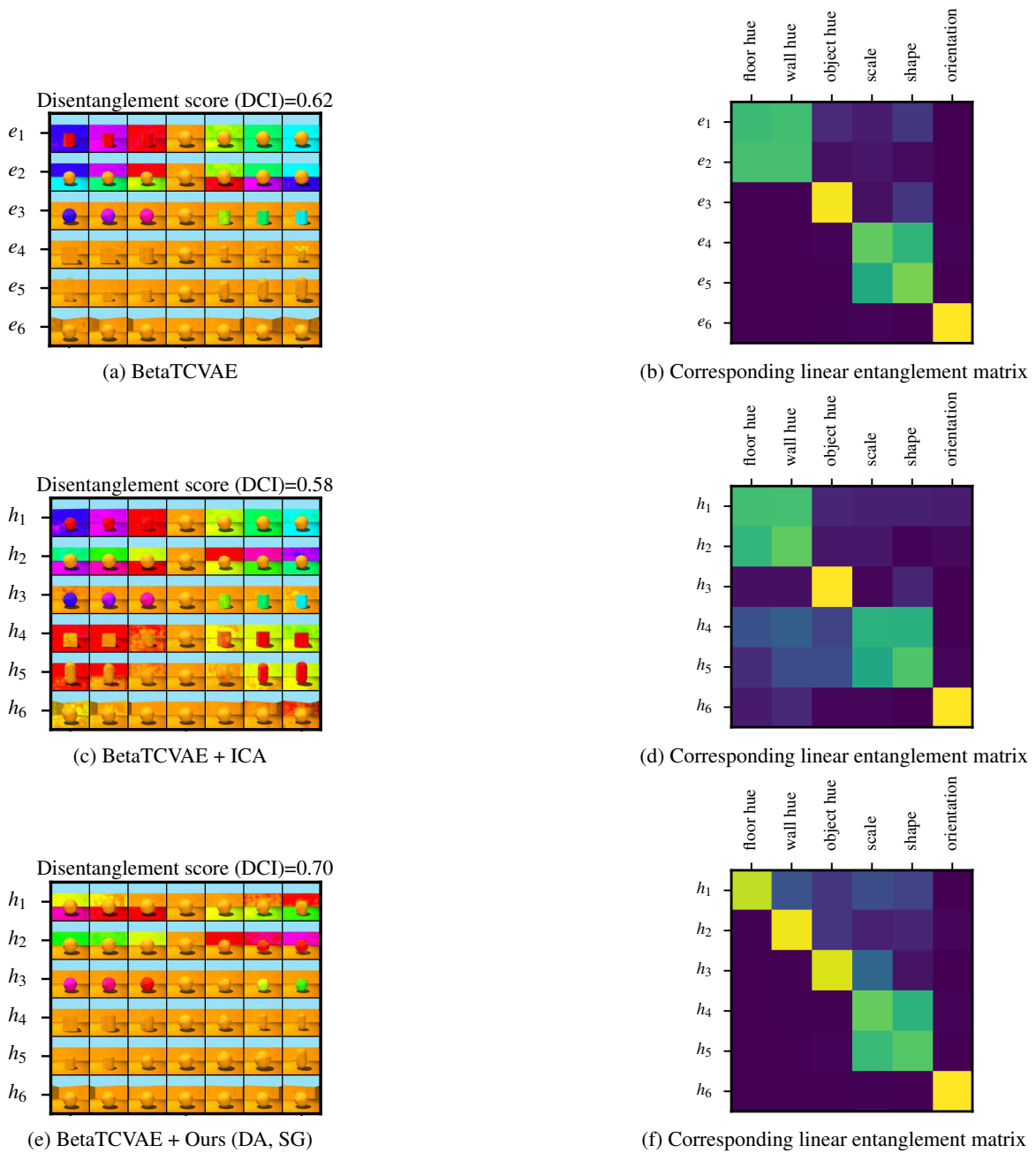


Figure 9: Traversal plots from another model (BetaTCVAE) trained on the correlated data set. As for all traversal plots in this paper, we manually permuted the dimensions to match across plots. In addition, we compute a matrix of linear entanglement that shows which ground truth factors is changed when moving into a certain direction (brightness corresponds to magnitude of change). While none of the post-hoc methods manages to disentangle shape and size (most likely due to their non-linear encoding), our model resolves the linearly entangled factors *floor hue* and *wall hue* fairly well, which can also be seen from the entanglement matrix.

## D.5 Further results on CUB

In Tab. 8, we report the quantitative comparison on CUB introduced in Appendix C.5 of our methods with PCA, ICA, and a baseline of randomly sampled directions. ICA failed to discover meaningful components, while PCA was only capable of discovering very few high-variance ones in the beginning, but begins to fail for  $K > 10$ . This is possibly because in PCA, the directions are required to be orthogonal. Surprisingly, both PCA and ICA were not much better than the random baseline. Our method constantly discovered components and surpassed all three baselines. In particular, our method (DA) with IG attributions leads to good performance. Figure 10 illustrates the correlation between the ground-truth attribute representation (scores) and predicted representation by using our model (using plain gradients) for the top discovered component. The two components are clearly correlated, but more in a block-sense: Classes with low scores on the attribute received low scores on the discovered component. The same holds for high scores, but within these, we observe stronger noise, which explains why the Spearman’s correlation values were imperfect. This can be due to a certain degree of arbitrage in the ground-truth attribute values of each class. Here, Fig. 11, just like Fig. 4 in the main paper, shows qualitative examples, including the ground-truth values which appear to fluctuate. We emphasize that this analysis should be viewed as a take on quantifying the quality of interpretable components, but that a refined benchmark is material for future work.

Num. components	K=1	K=10	K=20	K=30	K=40	K=50	K= 60
Baseline (random)	0.659 ± 0.017	0.618 ± 0.012	0.585 ± 0.011	0.559 ± 0.011	0.536 ± 0.010	0.516 ± 0.009	0.492 ± 0.010
PCA	<b>0.789</b> ± 0.024	0.602 ± 0.007	0.497 ± 0.005	0.440 ± 0.006	0.402 ± 0.004	0.372 ± 0.004	0.346 ± 0.004
ICA	0.515 ± 0.028	0.442 ± 0.005	0.412 ± 0.006	0.390 ± 0.007	0.370 ± 0.007	0.353 ± 0.007	0.335 ± 0.006
Ours-DA,Grad	0.701 ± 0.045	0.626 ± 0.029	0.585 ± 0.028	0.559 ± 0.011	0.535 ± 0.029	0.515 ± 0.030	0.490 ± 0.030
Ours-DA,IG	0.710 ± 0.020	<b>0.657</b> ± 0.008	<b>0.615</b> ± 0.013	<b>0.587</b> ± 0.016	<b>0.562</b> ± 0.018	0.539 ± 0.021	0.514 ± 0.021
Ours-DA,SG	0.686 ± 0.020	0.641 ± 0.031	0.610 ± 0.032	0.584 ± 0.032	0.561 ± 0.033	<b>0.540</b> ± 0.033	<b>0.516</b> ± 0.033

Table 8: Quantitative comparison of discovered components using our methods, PCA, ICA and a random baseline. Mean correlation score of top-K (K in column) discovered components are shown in (mean ± std.) for five runs. ”Ours-best” uses the best attribution method in each run. Bolt indicates the best result.

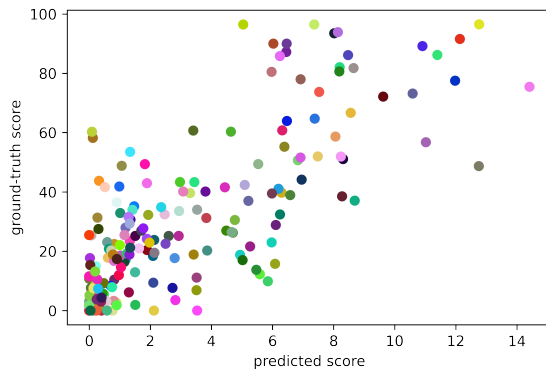


Figure 10: Correlation between ground-truth attribute scores and our predicted scores for the best matched component. Each dot represents a class.

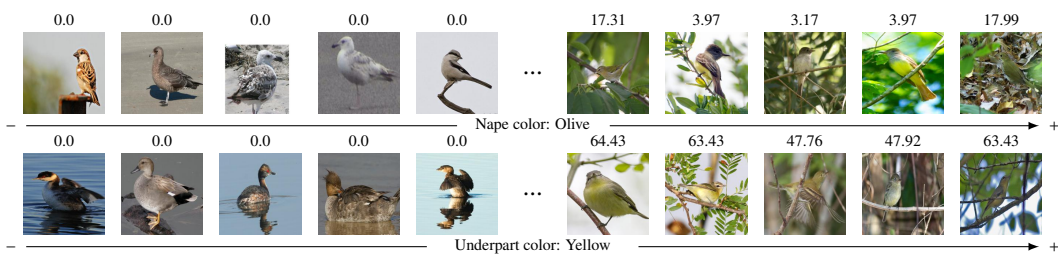


Figure 11: Examples of discovered components on CUB. The corresponding ground-truth attribute is shown under images and the ground-truth value of each image is depicted above the image. “+/-” indicate the positive/negative direction along the discovered concept.